DYNAMIC RELAXATION FOR INITIAL STRESS SETUP AND INELASTIC RESPONSE OF COMPLIANT FAULT ZONES TO THE NEARBY EARTHQUAKES

A Thesis

by

YOULI MAO

Submitted to the Office of Graduate and Professional Studies of
Texas A&M University
in partial fulfillment of the requirements for the degree of

MASTER OF SCIENCE

Chair of Committee,	Benchun Duan
Committee Members,	Judith Chester
	Richard Gibson
	Marcelo Sanchez
Head of Department,	Mike Pope

May 2017

Major Subject: Geophysics

ABSTRACT

In this thesis, we first develop a dynamic relaxation technique to obtain the initial stress field that is in static equilibrium for elastoplastic dynamic rupture models using a dynamic solver. Then we examine inelastic response of fault zones to nearby earthquakes. Our dynamic relaxation method mainly relies on a dynamic loading scheme that is applied on the model boundary. The main advantage of such an explicit dynamic relaxation is that the global mass matrix is diagonal. In addition, the global stiffness matrix is not explicitly assembled. There are two main steps in our dynamic relaxation method for obtaining the stress field in the inhomogeneous model: first, choose appropriate boundary nodal force loading for the homogeneous model to obtain the desired stress field; second, apply the same boundary nodal force loading to obtain the stress field for the same size but inhomogeneous model. Through the two steps, we present a viable approach to calculate stress field for inhomogenesous models.

We apply the dynamic relaxation technique to study the inelastic response of the Calico and Rodman fault zones to the 1992 Landers earthquake. We develop elastoplastic dynamic rupture models to study the rupture propagation and final slip distribution on the Landers faults. The initial stress field in the elastoplastic model is obtained through the dynamic relaxation method. We present the simulation results of the inelastic response in terms of residual displacement fields on the Earth's surface, and compare them with the InSAR observations in the East California Shear Zone. In addition, we compare our simulation results with those of elastic models from previous studies and show the advantage of elastoplastic models in term of data matching. The simulation results from our elastoplastic models show better match with the observed data compare to the results from previous elastic models.

ACKNOWLEDGMENTS

First and foremost, I would like to express my deep appreciation to Dr.Benchun Duan for all guidance and support during my graduate study. Dr.Duan gave me many great ideas for my research and continuously helped me on implementation with EQdyna library. I would like to thank Dr.Chester, Dr.Gibson and Dr.Sanchez for serving on my committee and presenting many insightful suggestions.

I would like to thank the professors and staff of the Department of Geology & Geophysics. Additionally, I would also like to thanks Ms.Dawson and Ms.Fike, who were graduate advisors during my graduate study. I also wish to express my gratitude to our research group member Dunyu Liu and Bin Luo for valuable discussions about the dynamic relaxation implementation.

Last, but most importantly, I would like to thank my wife, my daughter, my parents and my friends for their unconditional support, their encouragement and their confidence in me during the last three years.

CONTRIBUTORS AND FUNDING SOURCES

Contributors

This work was supported by the committee chair Dr.Duan. The numerical implementation in this work is based on the finite element code EQdyna developed by Dr.Duan. All the work conducted for the thesis was completed by the student independently.

Funding Sources

This work was funded in part by the National Science Foundation (NSF) and was also partly supported by the Southern California Earthquake Center (SCEC).

TABLE OF CONTENTS

LIST OF FIGURES

FIGURE Page

LIST OF TABLES

TABLE Page

1. INTRODUCTION

The compliant fault zones, also known as low velocity fault zones, are mainly composed of highly cracked and damaged rocks. The geometrical and mechanical properties of these fault zones can provide invaluable insight to understand the past earthquake ruptures and subsequent healing processes. For example, one can infer some mechanics of earthquake rupture from the responses, such as deformation information and degree of damage, of nearby compliant fault zones.

1.1 Background and literature review

Our focus will be on the response of compliant fault zones to nearby earthquakes, which has attracted substantial attention during the last two decades [e.g., Chester et al., 1993; Sleep, 1995; Chester and Chester, 1998; Ben-Zion and Sammis, 2003; Duan, 2010a]. Previous studies show that some port of the compliant fault zones shows inelastic response while the rest shows elastic response [e.g., Vidale and Li, 2003]. One of the major approaches in understanding the responses is to incorporate Interferometric Synthetic Aperture Radar (InSAR) observations into numerical modeling [e.g., Fialko et al., 2002; Fialko, 2004; Barbot et al., 2009]. However, it is still under debate whether the response should be elastic or elastoplastic [e.g., Duan et al., 2011; Duan, 2011].

In this thesis, we will investigate the inelastic response of Calico and Rodman fault zones to the 1992 Landers earthquake through comparison with InSAR anomalies in the same area. Our elastoplastic modeling mainly relies on the recent development of spontaneous rupture models [e.g. Duan, 2010a; Duan et al., 2011].

For the elastoplastic modeling, one important step is to figure out the initial stress field over the whole model region, especially within the compliant fault zone. Obtaining the initial stress filed through dynamic modeling is still very challenging from numerical

perspective. In fact, the author could not find any work related to initial stress field with compliant fault zone in current literature.

Here we propose an explicit dynamic relaxation approach to calculate the initial stress field when the entire model is in static equilibrium. The explicit dynamic relaxation method was initially proposed by Day [1965] for solving a static problem via a dynamic solver. The dynamic solver usually refers to the iterative method that integrating damping term, virtual mass and time stepping to solve a system until it reaches static equilibrium. We apply the finite element method to discretize the static equilibrium system [e.g. Duan and Oglesby, 2006; Duan and Day, 2008; Duan, 2010a,b; Duan et al., 2011]. Such discretization comes with two computational advantages: the global mass matrix is diagonal and there is no need to explicitly assemble the global stiffness matrix. The two advantages largely improve the computation efficiency and make it feasible to attack large systems.

The main ingredient into our explicit dynamic relaxation method is a boundary loading scheme that applied to the model till it reaches static equilibrium. By static equilibrium, we refer to both the acceleration and velocity of the system approach zero after certain period of time. In the boundary loading scheme, we apply appropriate nodal force on the boundary finite element nodes to obtain the desired stress field. It comes with two steps: first, find appropriate boundary nodal force loading for the homogeneous model; second, apply the same boundary loading to the similar model with compliant fault zones.

After the system reaches static equilibrium, the stress field over the whole model region is generated and will set as input in the elastoplastic dynamic rupture modeling. In the elastoplastic dynamic rupture modeling, Drucker-Prager yield criterion is implemented in determining the material failure [e.g. Drucker and Prager, 1952]. In addition, the slip weakening law is implemented to control the rupture propagation [e.g. Ida, 1972; Andrews, 1976]. We perform a large amount of parameter tests based on the seismic S value introduced in Day [1982] and stress drop to obtain the reasonable rupture propagation and

final slip distribution on fault. By reasonable we mean that our simulation results on rupture propagation and final slip distribution are consistent with the inversion results of the Landers earthquake reported in previous studies [e.g. Cohee and Beroza, 1994; Wald and Heaton, 1994].

Finally, we perform two similar numerical model and take the difference to emphasize the response merely caused by material difference between compliant fault zones and host rocks. We will further compare our simulation results with the InSAR observations of East California Shear Zone (ECSZ) reported in literature [e.g. Cochran et al., 2009; Barbot et al., 2009].

1.2 Outline of the thesis

The thesis is organized as follows:

1. In Section 2.1, we introduce the fixed end beam model with analytical solution to verify our dynamic relaxation technique. Then we implement it and show the numerical results as well as compare with analytical solution. This section ends with a brief discussion on the accuracy of numerical modeling.

2. In Section 2.2 , we apply the boundary loading technique into the homogeneous earth model to obtain the desired stress field. The numerical results and discussion will be presented in the end of this section.

3. In Section 2.3, we add a low velocity fault zone into the same size earth model in Section 2.2 and perform the same boundary loading force to obtain the stress field over the whole model region. Substantial numerical experiments are presented at the end of this section.

4. In Section 3.1, we present the modeling for the Landers earthquake as well as two nearby compliant fault zones: Calico and Rodman. We then introduce the veloc-

ity structure for the compliants fault zones and the corresponding stress field after dynamic relaxation.

5. In Section 3.2, we present the results of rupture propagation and final slip distribution on fault in our numerical modeling.

6. In Section 3.3, we first show our simulation results of the response of Calico and Rodman fault zones to the Landers rupture. Then we compare them with InSAR data and present a brief discussion in the end of this section.

7. Finally, summary of this thesis as well as some discussions on future work are reported in Section 4.

2. DYNAMIC RELAXATION

Dynamic relaxation method provides a way to simulate the actual process of how the system evolves to static equilibrium during a transient period. The key idea in dynamic relaxation is to convert a time-independent static problem into a dynamic one via introducing an inertia term in the equation of motion. The small displacement elastodynamics is governed by the equation of motion:

$$\nabla \cdot \boldsymbol{\sigma} + \mathbf{b} = \rho \ddot{\mathbf{u}} \tag{2.1}$$

where $\boldsymbol{\sigma}$ is the stress tensor, $\mathbf{b}$ is the body force vector, ρ is the mass density, $\ddot{\mathbf{u}}$ is the two time derivative of global displacement.

Space-time finite element methods are applied to obtain a semidiscrete matrix equation [e.g. Belytschko et al., 1995; Hughes and Hulbert, 1988; Hulbert and Hughes, 1990]. The equation of motion is discretized in the follow way:

$$\mathbf{M}\ddot{\mathbf{u}} + \alpha \mathbf{M}\dot{\mathbf{u}} + \mathbf{K}\mathbf{u} = \mathbf{M}g + \mathbf{F}_{ext} \tag{2.2}$$

where $\mathbf{M}$ denotes the global mass matrix and $\mathbf{K}$ denotes the global stiffness matrix, $\mathbf{F}_{ext}$ denotes the external loading, α denotes the damping coefficient, $\mathbf{u}$ denotes the global displacement vector, g is gravitational acceleration, $\ddot{\mathbf{u}}$ and $\dot{\mathbf{u}}$ represent the corresponding global acceleration and velocity vector, respectively.

The nodal elastic restoring force vector $\mathbf{f} = \mathbf{K}\mathbf{u}$ in Equation (2.2) is found directly from the stress tensor $\boldsymbol{\sigma}$ without assembling the stiffness matrix $\mathbf{K}$ by applying operator $\mathcal{F}$ to the stress, i.e. $\mathcal{F}(\boldsymbol{\sigma}) = \mathbf{K}\mathbf{u}$. Now let $\mathbf{L}$ be the operator that operates on the global displacement vector to generate stress, the equations are then of the form:

$$\dot{\mathbf{v}} = -\alpha\mathbf{u} - \mathbf{M}^{-1}[\mathcal{F}(\boldsymbol{\sigma}) - \mathbf{M}g - \mathbf{F}_{ext}] \tag{2.3}$$

$$\dot{\mathbf{u}} = \mathbf{v} \tag{2.4}$$

$$\boldsymbol{\sigma} - \mathbf{L}(\mathbf{u}) = 0 \tag{2.5}$$

when the system reaches static equilibrium, we obtain

$$\mathcal{F}(\boldsymbol{\sigma}) - \mathbf{M}g - \mathbf{F}_{ext} = 0 \tag{2.6}$$

$$\dot{\mathbf{u}} = 0 \tag{2.7}$$

$$\boldsymbol{\sigma} - \mathbf{L}(\mathbf{u}) = 0 \tag{2.8}$$

Give some approximation $\tilde{\boldsymbol{\sigma}}$ to the equilibrium stress, plug into Equation (2.6) to get the residual $r(\tilde{\boldsymbol{\sigma}})$

$$r(\tilde{\boldsymbol{\sigma}}) = \mathcal{F}(\boldsymbol{\sigma}) - \mathbf{M}g - \mathbf{F}_{ext} \tag{2.9}$$

We then apply a simple iteration to solve Equation (2.6)-(2.8) by plug Equation (2.9) into Equation (2.3):

$$\dot{\mathbf{v}} = -\alpha\mathbf{v} - \mathbf{M}^{-1}r(\tilde{\boldsymbol{\sigma}}) \tag{2.10}$$

then solve with Equation (2.10) with Equation (2.4) and (2.5) until $\mathbf{v} = 0$, at which point the residual will be zero.

This can be done by splitting the Equation (2.3)-(2.5) and iterating a simple Euler-explicit calculation:

$$\boldsymbol{\sigma}^j = \mathbf{L}(\mathbf{u}^j) \tag{2.11}$$

$$\mathbf{v}^{j+1} = (1 + \alpha\triangle t)\mathbf{v}^j - \mathbf{M}^{-1}\triangle t[\mathcal{F}(\boldsymbol{\sigma}) - \mathbf{M}g - \mathbf{F}_{ext}] \tag{2.12}$$

$$\mathbf{u}^{j+1} = \mathbf{u}^j + \triangle t\mathbf{v}^{j+1} \tag{2.13}$$

where the approximation solution $\tilde{\boldsymbol{\sigma}}$ thus takes a successive values $\boldsymbol{\sigma}^j, j = 1, 2, 3, ...$ When the residual $r(\tilde{\boldsymbol{\sigma}})$ reaches a small enough stoping criteria (the system is in static equilibrium), we stop the iteration and obtain the desired stress field over the whole model region.

The proposed dynamic relaxation method mainly relies on the exterior loading $\mathbf{F}_{ext}$ in Equation (2.2). Specifically, the exterior loading $\mathbf{F}_{ext}$ is given by appropriate nodal force loading on the model boundary. Furthermore, the boundary nodal force loading is continuously applied on the model boundary until the system reaches static equilibrium. The implementation of the proposed algorithm is modified based on the community verified finite element code EQdyna [e.g. Duan and Oglesby, 2006; Duan and Day, 2008; Duan, 2010a,b; Duan et al., 2011]. The code was developed by Dr.Duan, which mainly focus on the numerical simulation of 3D dynamic rupture and seismic wave propagation in inhomogeneous elastoplastic media.

For the equation of motion (2.1), there are typically three boundary conditions: first, Dirichlet boundary condition, which specifies the values on the solution itself on the boundary, and it is also known as essential boundary condition; Second, Neumann boundary, which specifies the values of the derivative of the solution, and it is also known as natural boundary condition; third, Robin boundary condition, which is the combination

of Dirichlet and Neumann boundary condition. For different tests, we choose different boundary condition setup to perform different numerical experiments.

In order to verify the implementation, we perform a set of numerical experiments of different physical models.

2.1 Fixed end beam model

First, we perform numerical experiment on a classic fixed end beam problem, in which one end of the beam is subjected to a shear bending. In this test, we fix one end of the beam on the wall and load the other end by concentrated load as shown in Figure 2.1. In our implementation, we first mark the different boundary types and assign the corresponding boundary conditions for the physical model.

The properties of material are given as follows:

1. Density: $\rho = 7.8 \times 10^3\ kg/m^3$
2. Young's modulus: $E = 2.1 \times 10^{11}\ Pa$
3. Poisson coefficient: $\nu = 0.29$

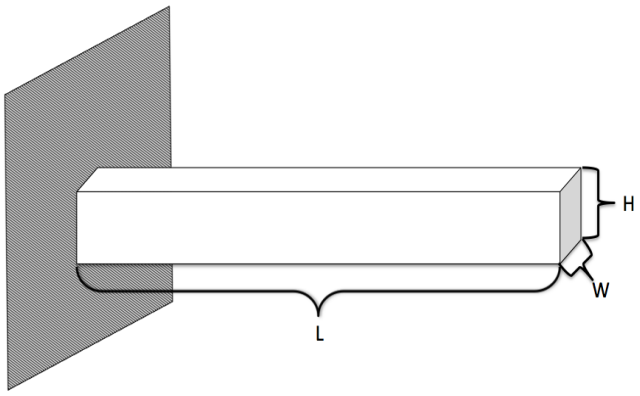

Figure 2.1: Physical model of the beam problem

We set the same materials parameters in our code and perform the numerical experiments. The analytical solution of the fixed end beam problem is given in Timoshenko and Gere [1972]:

$$\frac{d}{L} = \frac{FL^2}{3EI},\ where\ \ I = \frac{WH^3}{12} \tag{2.14}$$

where F is the boundary loading force, E is the Young's modulus of the beam, L is the length of the beam, W is the width of the beam, H is the height of the beam, d is the vertical displacement of loading end of the beam as shown in Figure 2.2.

Loading	d_a/L (analytical)	d_n/L (numerical)	Error
Test 1	2.0×10^{-3}	2.08×10^{-3}	3.0%
Test 2	4.0×10^{-3}	4.10×10^{-3}	2.5%
Test 3	6.0×10^{-3}	6.20×10^{-3}	3.3%
Test 4	8.0×10^{-3}	8.15×10^{-3}	1.9%
Test 5	1.0×10^{-2}	1.02×10^{-2}	2.0%
Test 6	1.2×10^{-2}	1.23×10^{-2}	2.5%

Table 2.1: Comparison between numerical and analytical results

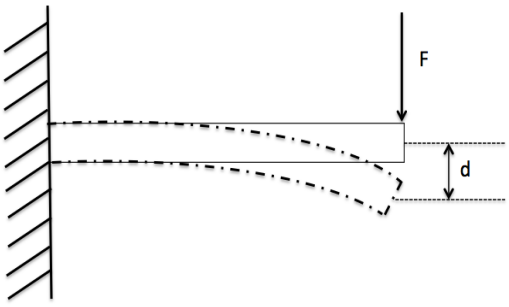

Figure 2.2: Bending after boundary loading

In order to verify the implementation, we test six different linearly increased loading forces on the right end of the beam and record the corresponding vertical displacements as shown in Table 2.1. Here the numerical error is calculated by the formula:

$$Error = |\frac{d_a/L - d_n/L}{d_a/L}| \tag{2.15}$$

We also plot the comparison between numerical and analytical results in Figure 2.3. From the comparison in Table 2.1, one can observe that the numerical results remain quite close to the analytical solution with error less than 5%. In addition, the numerical results are also robust with different mesh size in the finite element method.

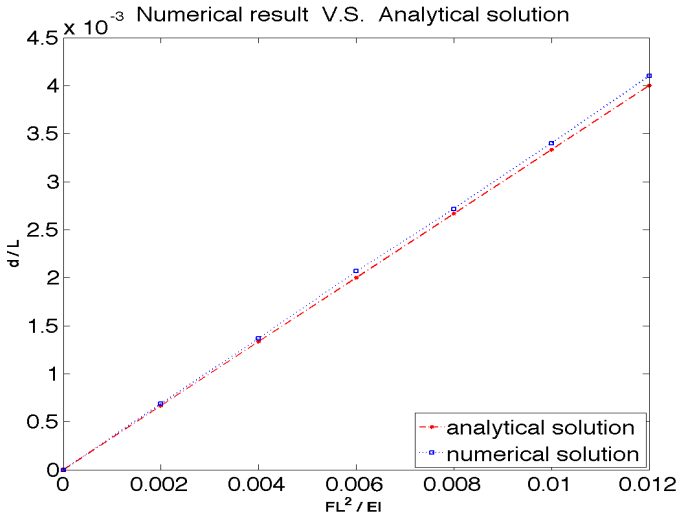

Figure 2.3: Comparison between numerical and analytical solution

In this section, we have successfully verified the dynamic relaxation method based on boundary loading scheme with a classical fixed beam problem with analytical solution. We presented the comparison between the analytical solution and numerical solution as well as the corresponding error analysis.

2.2 Boundary loading earth model

The purpose of this thesis is to find the stress field for the earth model, especially for the model with compliant fault zones. In general, there are two steps in finding the stress status inside the low velocity fault zones. The first step is to find the designed stress status

for homogeneous material with appropriate boundary nodal force loading. The second step is to apply the same nodal force loading on the first step to the inhomogeneous earth model (with low velocity fault zone inside). Note that many physical parameters in the models in step one and step two remains the same, except the P-wave and S-wave velocity.

In this section, we mainly focus on the first step which is to find the desired global stress status over the whole model region by boundary loading as shown in Figure 2.4.

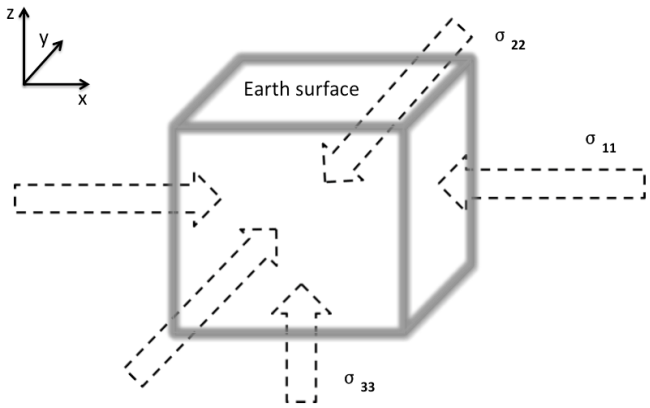

Figure 2.4: Homogeneous Earth model with boundary nodal force loading

In this test, we want to obtain the following stress status over the whole model region:

$$\sigma_{11} = 1.25\sigma_{33} \tag{2.16}$$

$$\sigma_{22} = 0.75\sigma_{33} \tag{2.17}$$

$$\sigma_{12} = -0.433\sigma_{33} \tag{2.18}$$

$$\sigma_{13} = \sigma_{23} = 0 \tag{2.19}$$

Note that here σ_{11} refers to σ_{xx} in the 3D Cartesian coordinate system, so on so forth.

The material parameters of the model in this test are given as follows:

1. Density: ρ = 2.67$\times 10^3$ kg/m^3
2. P-wave velocity: V_P = 6.0 $\times 10^3$ m/s
3. S-wave velocity: V_S = 3.464 $\times 10^3$ m/s
4. damping coefficient α: 0.15

Other parameters such as bulk modulus, shear modulus, Lame's coefficient, Young's modulus, Poisson's ratio and P-wave modulus can be calculate based on the above parameters. Note that this model is elastic and plastic deformation is not allowed here. In addition, there is no fault within the model. Hence, we do not introduce the internal frictional coefficient and cohesion of the material here.

The geometry information of the 3D is given by $20\ km\ \times 20\ km\ \times 20\ km$ where $X_{coor} \in [-10\ km, 10\ km]$, $Y_{coor} \in [-10\ km, 10\ km]$ and $Z_{coor} \in [0\ km, -20\ km]$. In the space-time finite element setup, we set $dx = 500m$ and $dt = 0.03s$ ($dt \leq \frac{dx}{V_p}$) in order to avoid the numerical stability issue. Selection of appropriate nodal force loading is the key to obtain the desired stress status. We refer to the definition of stress as the load per unit area shown in Equation (2.20):

$$Stress : \sigma = \frac{F}{A} \Longrightarrow F = \sigma \cdot A \tag{2.20}$$

where F is the loading force, A is the cross sectional area.

The loading force is applied on the finite element nodes on the model boundary (see Figure 2.5). In Figure 2.5, we use a mini finite element model (eight elements in total) to depict the nodes on the boundary. According to Equation (2.20), stress is defined based on the force applied per unit area. Each face of one element has four nodes and nodes in different position may contribute differently to that face when applied nodal force loading.Depending on the various positions, these boundary finite element nodes can be divided into three different categories: (i) interior boundary nodes, (ii) planar interception nodes (exclude corner nodes) and (iii) corner nodes. For the interior boundary nodes marked in red in Figure 2.5, each one is shared by four elements in that boundary plane and there are four such nodes in the face of such element, thus the loading force on that element face should be $Stress \times Area$. For the planar interceptions boundary nodes marked green in Figure 2.5, each node is shared by two elements on that plane (e.g. x-z plane or y-z plane), thus the nodal loading force on such element should be $\frac{1}{2} \times Stress \times Area$. For the corner boundary nodes marked in yellow in Figure 2.5, each node only belong one element on each plane (e.g. x-z plane), thus the loading force on that plane should be $\frac{1}{4} \times Stress \times Area$.

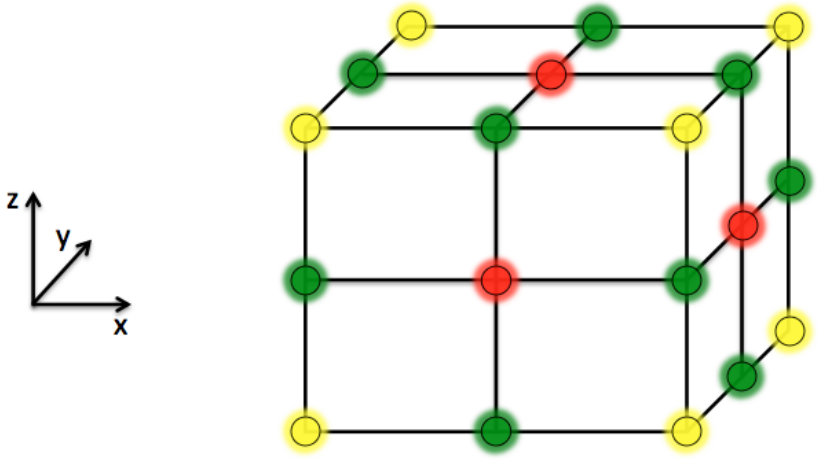

Figure 2.5: Finite element nodes on the model boundary. In the showcase, there are only eight finite elements with three different types of boundary nodes on face, edge and corner of the model, respectively.

The following are the boundary loading force on each plane:

On the boundary parallel to Y-Z plane ($X_{coor} = X_{min}$ & X_{max})

i. $F_{normal\ dir} = 1.25 \times \rho \times g \times |zcoor| \times dy \times dz$,

ii. $F_{shear\ dir} = -0.433 \times \rho \times g \times |zcoor| \times dy \times dz$

On the boundary parallel to X-Z plane ($Y_{coor} = Y_{min}$ & Y_{max})

i. $F_{normal\ dir} = 0.75 \times \rho \times g \times |zcoor| \times dx \times dz$,

ii. $F_{shear\ dir} = -0.433 \times \rho \times g \times |zcoor| \times dx \times dz$

On the bottom of the model ($Z_{coor} = Z_{min}$ & Y_{max})

i. $F_{normal\ dir} = \rho \times g \times |zcoor| \times dx \times dy$,

In addition to model boundary nodes, the boundary between Message Passing Interface (MPI) partitions also need special treatments. In our implementation, the version of EQdyna has been paralleled with MPI along X-axis. These MPI boundary nodes can be categorized into type (ii) as planer interceptions. In Figure 2.6, we show an example of boundary nodes between the MPI partitions along X-axis.

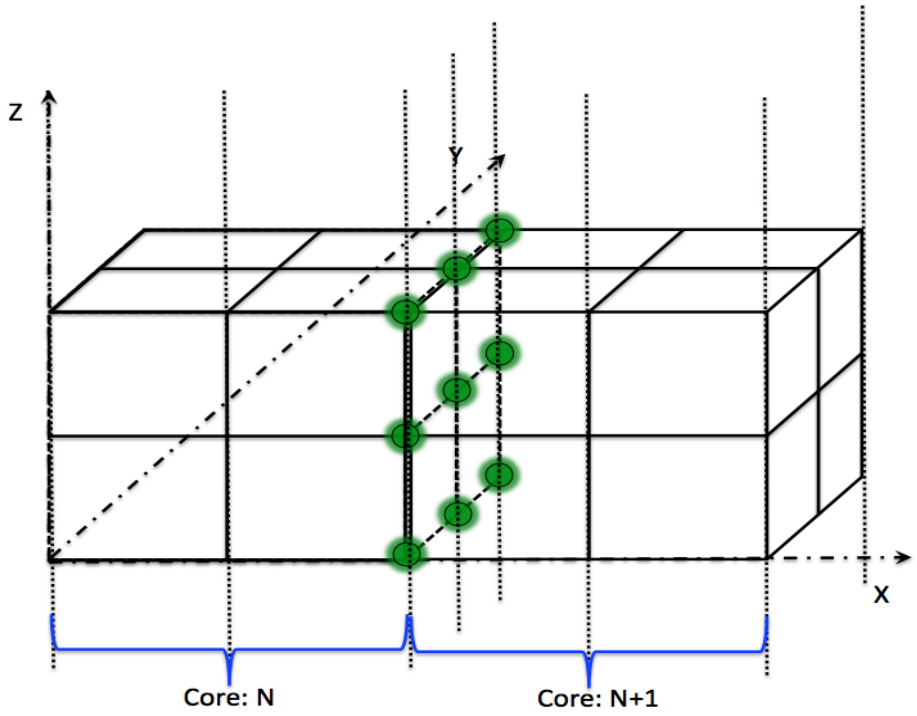

Figure 2.6: Finite element nodes on MPI interface of the model. In this showcase, there is one type of nodes between MPI partitions which do not overlap with model boundary.

After the appropriate boundary nodal force loading, we plot them in terms of vectors

over the whole model. Note that the magnitude of loading force is depth dependent as shown in Figure 2.7.

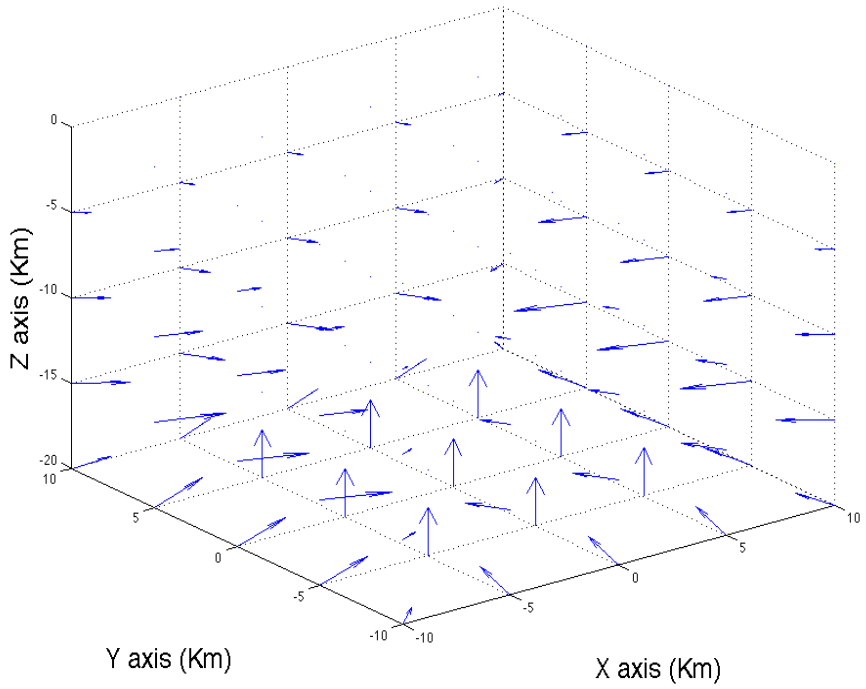

Figure 2.7: Vector field of the boundary nodal force loading of the homogeneous Earth model, there are 64 finite elements in total and 56 elements on the model boundary.

After the system reaches the stop criteria of static equilibrium, we obtain the stress field over the model. We observe that the stress status is almost identical on different cross section layers of finite element over the whole model region as expected. In order to visualize the stress field, we plot the element stress of one cross section layer of elements (in $Y - Z$ plane) in the model shown in Figure 2.8.

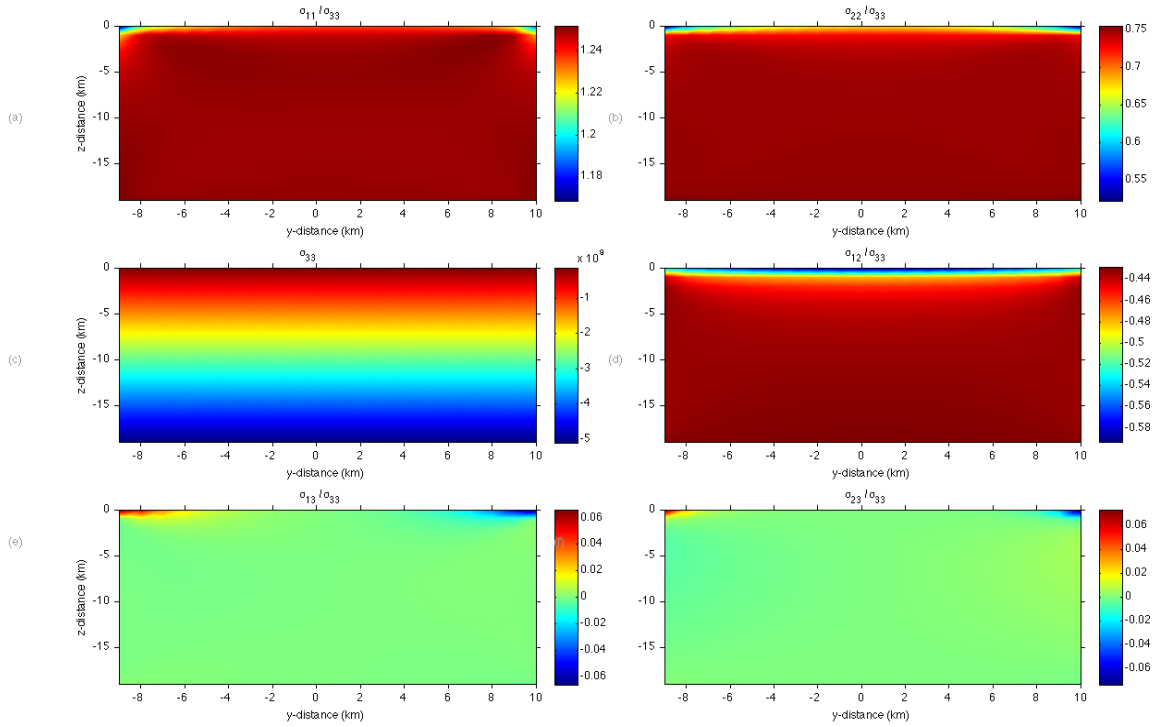

Figure 2.8: Cross section of stress status with free surface loading normalized by σ_{33}. σ_{11} corresponding to σ_{xx}, σ_{22} corresponding to σ_{yy} and σ_{33} corresponding to σ_{zz}, respectively.

From both Figure 2.8, one can observe that the stress field after dynamic relaxation over the model region is very close to the desire stress field. Note that the stress field on the top layer of finite element is not quite satisfactory due to the fact that Z_{coor} corresponding to surface nodes is 0. Hence, the boundary loading on surface is 0 according to depth dependent loading scheme. In order to improve the stress field on surface, we assign an artificial depth to the surface node, namely $\beta \cdot dz$ (where $\beta \in (0, 1)$, $\beta = \frac{1}{3}$ in the results showing in Figure 2.9). By applying appropriate artificial surface loading, we improve the desired stress field on the surface finite element layer as shown in Figure 2.9.

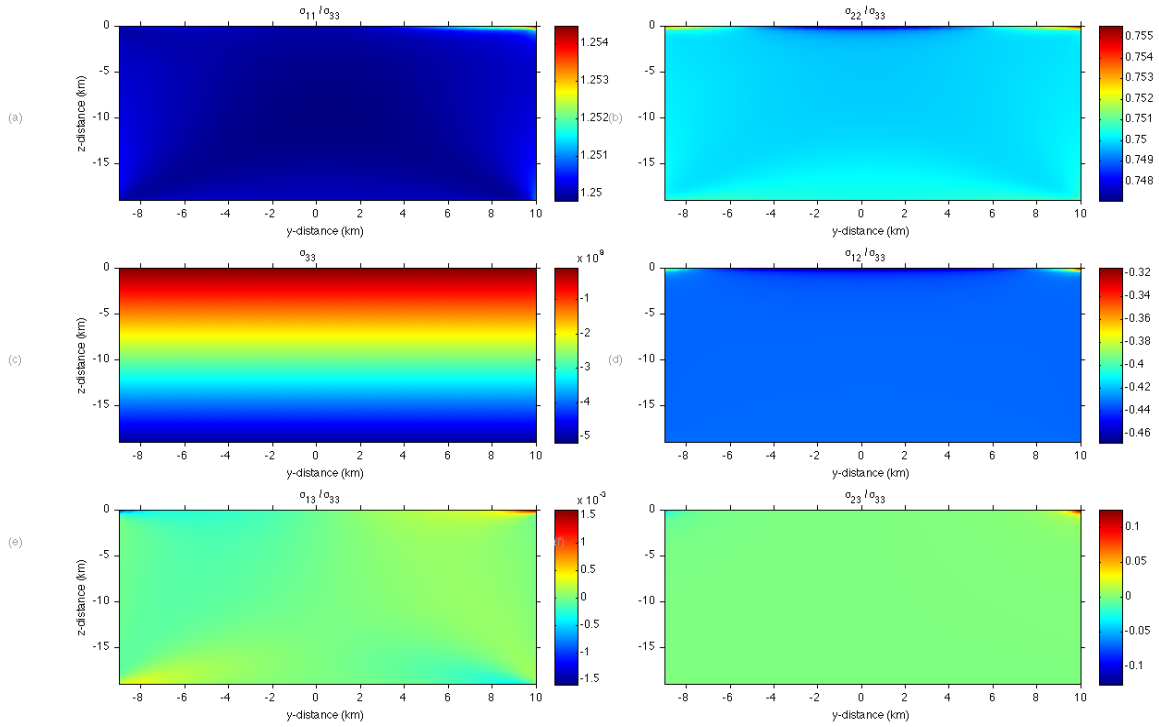

Figure 2.9: Cross section of stress status with appropriate surface loading normalized by σ_{33}. σ_{11} corresponding to σ_{xx}, σ_{22} corresponding toσ_{yy} and σ_{33} corresponding to σ_{zz}, respectively.

During the numerical experiments, we found that the damping coefficient plays an important role, especially in term of time duration needed to reach static equilibrium. We run several tests to examine the damping effect on the same system during the dynamic relaxation process as shown in Figure 2.10.

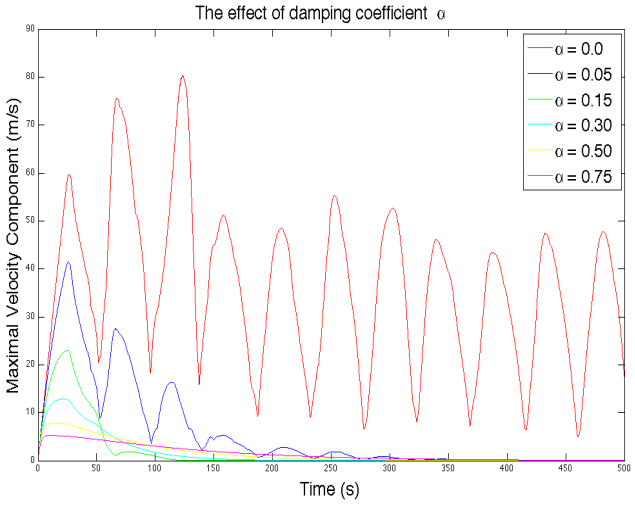

Figure 2.10: Effect of damping coefficient in the dynamic relaxation process, in which one can find an optimal value for the system to take least time.

One can observe that neither too small nor too large damping coefficient is optimal for the system to reach static equilibrium in the shortest duration as shown in Figure 2.10. In this numerical model, $\alpha = 0.15$ is the optimal value which take the least time to get the system in static equilibrium.

In this section, we have applied the boundary loading technique into obtaining desired stress field for the homogeneous model. In numerical experiments, we showed that the proposed scheme is efficient and robust, thus making our method a feasible tool for obtaining model stress field.

2.3 Stress field for model with compliant fault zone

For the model with homogeneous material, our boundary loading scheme has been successfully verified. The first step of obtaining the stress field for the model with inhomogeneous material (e.g. models contain compliant fault zone) has been accomplished.

The next step is to apply the same boundary loading to the same size inhomogeneous model as shown in Figure 2.11.The compliant fault zones, also known as low velocity fault zones, are composed of fractured and damaged rocks, where the body wave velocity has been largely reduced. The geometrical information of compliant fault zones can be used to infer the mechanics of past earthquake ruptures due to the fact that rocks near fault core are weakened by micro-fracture events, such as micro-cracking and coalesce of micro-joints, during dynamic rupture propagation and stress perturbation [e.g. Scholz et al., 1993; Chester et al., 1993; Chester and Chester, 1998]. For example, the width of compliant fault zones is a function of total fault displacement [e.g. Savage and Brodsky, 2011]. In order to study the geometrical and mechanical properties of the compliant fault zones, such as width, depth and rigidity reduction, there have been several attempts in the past to incorporate the seismic fault zone waves and their corresponding travel time analysis for imaging low-velocity structures [e.g. Ben-Zion, 1998; Li et al., 1998; Ben-Zion and Sammis, 2003]. In addition, Interferometric Synthetic Aperture Radar (InSAR) technique has also been applied to study the geologic structure of the compliant fault zones and their responses to the nearby earthquakes [e.g Fialko et al., 2002; Fialko, 2004; Barbot et al., 2009]. For the width of the compliant fault zones, seismic studies indicates that it is in the range of hundred meters while the InSAR studies indicates that it is in the range from one to several kilometers. For the depth of the compliant fault zones, seismic studies shows that the damaged fault zone are limited to shallow features of top several kilometer while InSAR studies imply that it could be extended to several kilometers deep, even the entire seismogenic zone. For the seismic velocity reduction, seismic studies suggest that the reduction is in the range 20% - 40% while InSAR studies suggest that when the reduction is between 40% to 50% the numerical model fits the observation best. In this thesis, we will model adapt the width and depth of compliant fault zones suggested by InSAR studies since our ultimate goal is to compare our numerical results with the InSAR observation

data. In this numerical model, we set the compliant fault zone to be 3.6 km wide and 2 km deep, the velocity reduction within the compliant is 40% compare to the host rock.

We marked the compliant fault zone in blue in Figure 2.11, which is about a few kilometers under the surface of the model. It locates in the middle of the model along Y-axis and across the whole model along X-axis.

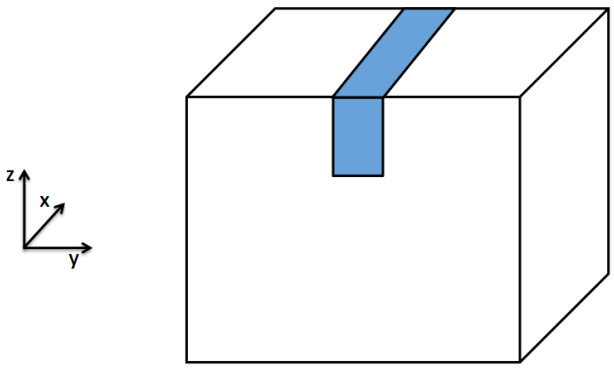

Figure 2.11: Earth model with low velocity fault zone, which is marked in blue on the top of the model.

The material parameters of the compliant fault zone in our numerical experiment are given as follows:

1. Density: $\rho = 2.67 \times 10^3\ kg/m^3$
2. P-wave velocity: $V_P = 2.4 \times 10^3\ m/s$
3. S-wave velocity: $V_S = 1.368 \times 10^3\ m/s$

Similar to the homogeneous model, this model is also elastic and no plastic deformation is allowed here. So the internal frictional coefficient and cohesion of material is not

introduced here either.

It is clear that velocity of body waves is much smaller within the low velocity fault zone.The difference in P-wave and S-wave velocity will lead to other different material physical properties, such as Young's modulus, Poisson ratio, etc. It will cause inhomogeneous stress distribution around the low velocity fault zone when applying boundary loading force. After the system reaches static equilibrium, we plot the one cross section layer of finite element in the model to examine the stress status. Since the low velocity fault is located in the middle of the model along Y-axis, it is better to take the Y-Z cross section layer for visualization purpose. In addition, the stress field of these cross section layers along X-axis is very similar because of the symmetry of the model.

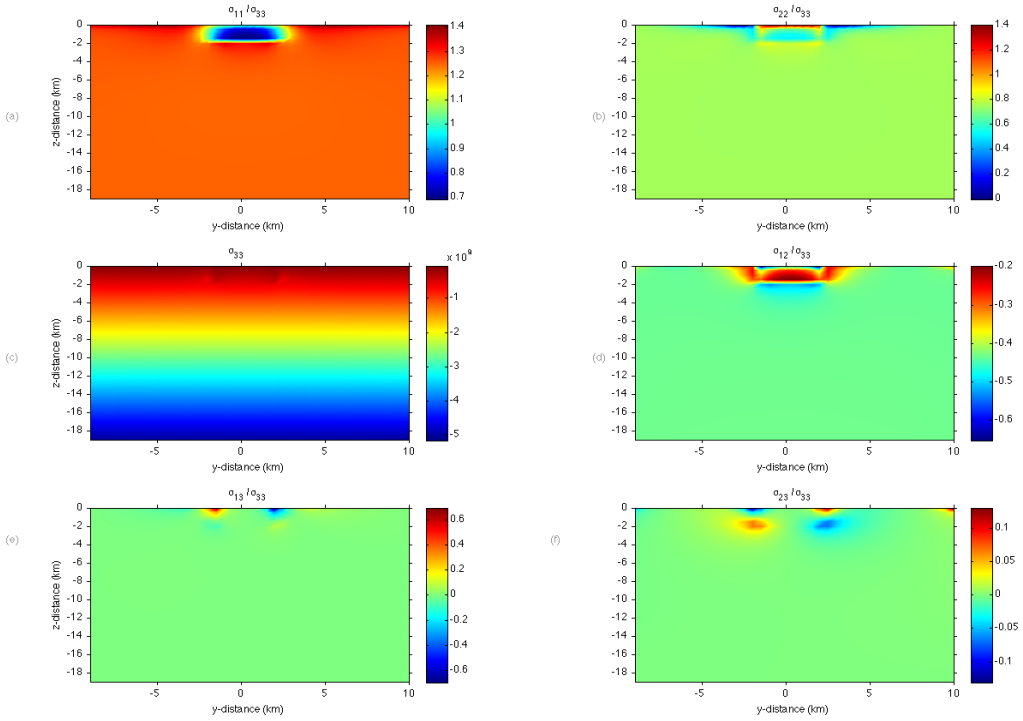

Figure 2.12: Shallow low velocity fault zone. Cross section of stress status with free surface loading normalized by σ_{33}. σ_{11} corresponding to σ_{xx}, σ_{22} corresponding to σ_{yy} and σ_{33} corresponding to σ_{zz}, respectively.

From Figure 2.12, one can observe obvious stress heterogeneity around the low velocity fault zone. The stress field for the rest of the model remains the preserved relation as in step one. In addition, the stress ratio within the compliant fault zone is relatively low compare to that in the intact rocks. The reason is that compliant fault zone has relatively small deformation compare to that in the intact rock when applying boundary loading due to the difference in physical properties. In order to further study the effect of low velocity fault zone location on global stress distribution, we perform several numerical experiments with low velocity fault zone on different depth of the model. We set its depth

to be $Z_{coor} \in [-2\ km, -4\ km]$ and $Z_{coor} \in [-10\ km, -12\ km]$ as shown in Figure 2.13 and Figure 2.14.

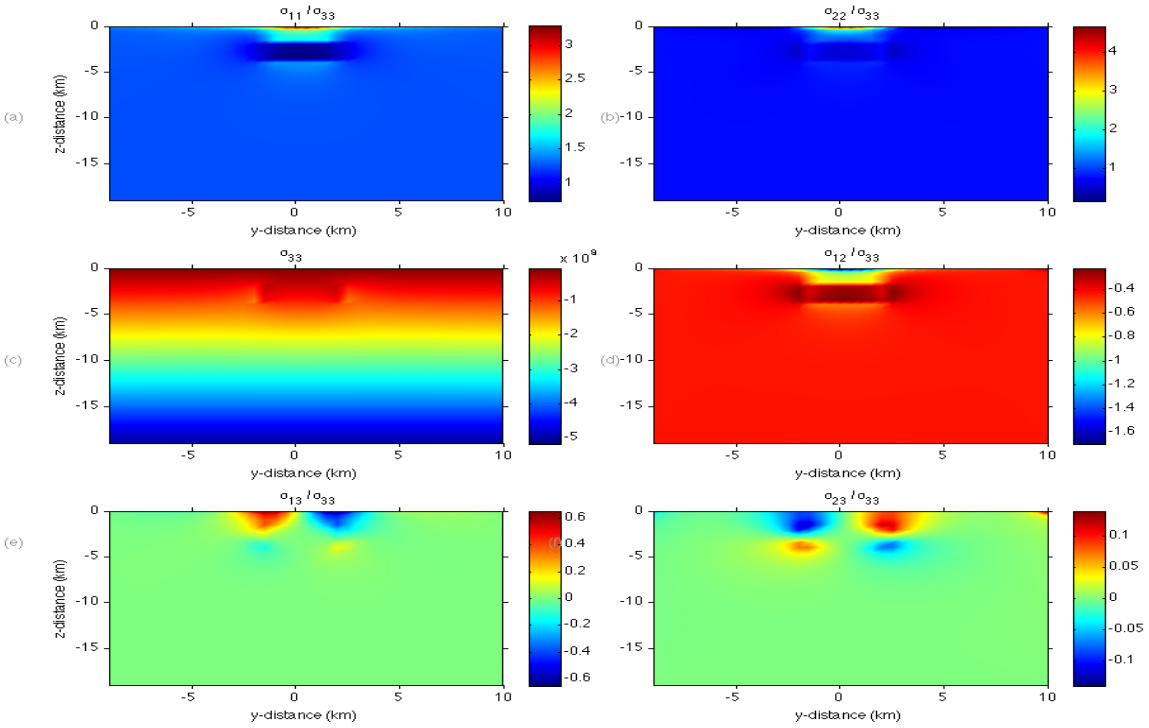

Figure 2.13: Middle depth low velocity fault zone. Cross section of stress status with free surface loading normalized by σ_{33}. σ_{11} corresponding to σ_{xx}, σ_{22} corresponding to σ_{yy} and σ_{33} corresponding to σ_{zz}, respectively.

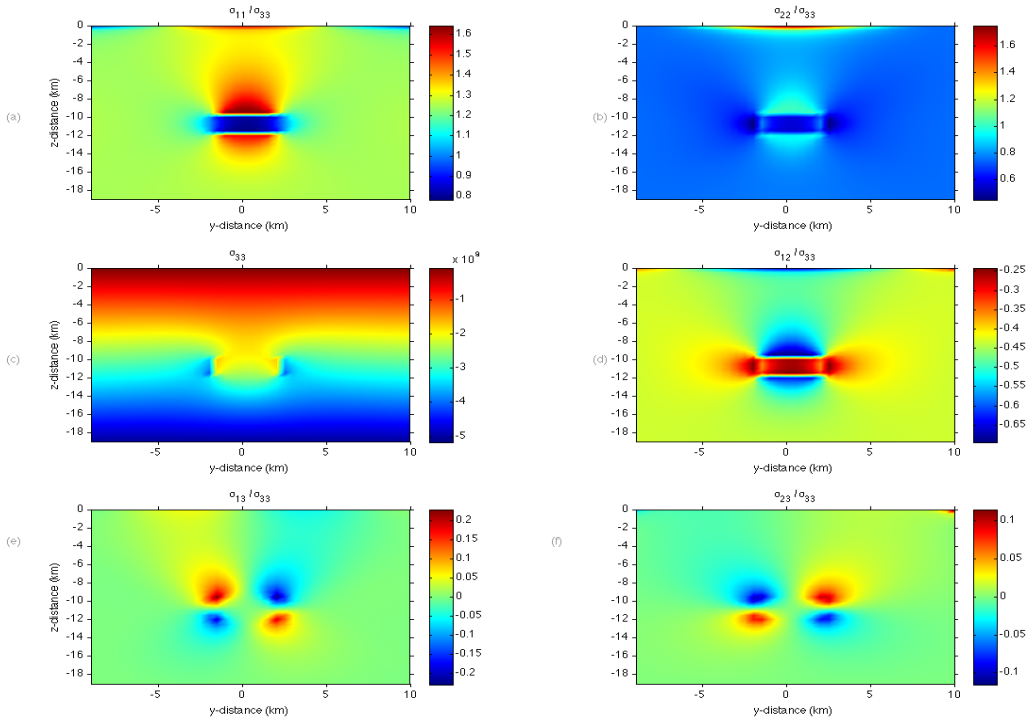

Figure 2.14: Deep low velocity fault zone. Cross section of stress status with free surface loading normalized by σ_{33}. σ_{11} corresponding to σ_{xx}, σ_{22} corresponding to σ_{yy} and σ_{33} corresponding to σ_{zz}, respectively.

From Figure 2.13 and Figure 2.14, one can observe that the depth of low velocity fault zone indeed affect its surrounding stress status. The impact of low velocity fault zone on surface stress heterogeneity always exists, independent of depth. Considering the fact that the boundary loading is depth dependent, the deeper the low velocity fault is, the larger the impact area inside the model is.

In order to fit InSAR data better, Cochran et al. [2009] suggested to apply a gradually reduced velocity within the compliant fault zone (shown in Figure 2.15) which provides the best result.

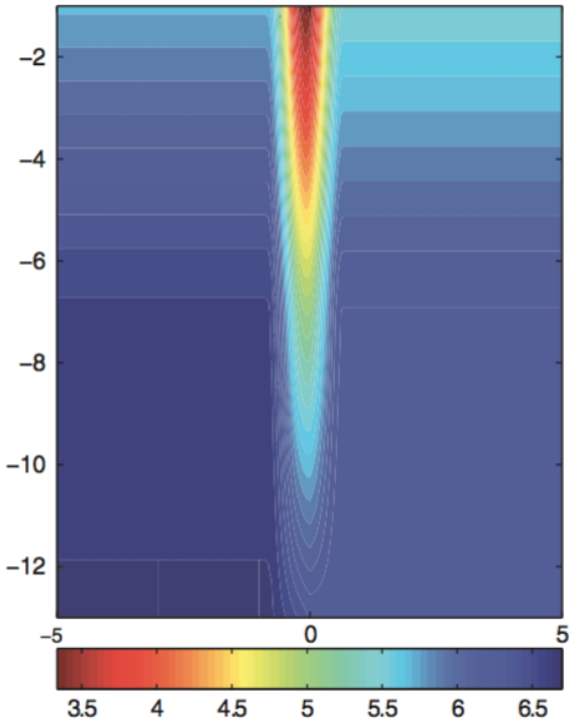

Figure 2.15: Velocity structure of compliant fault zone reported in Cochran et al. [2009]

Following their idea, we will test different velocity structures within the damaged fault zones to study their impacts on the stress field when the model reaches static equilibrium. One can observe that the velocity structure does affect the stress change around the compliant fault zone.

For example, the ratio σ_{11}/σ_{33} ranges from 0.6 to 1.8 on the interface between the low velocity fault zone and its host rock as shown in Figure 2.14 (a); the ratio σ_{12}/σ_{33} range from -0.65 to -0.25 on the interface between the low velocity fault zone and its host rock as shown in Figure 2.14 (d).

Now we will implement the idea of gradually changed velocity structure for the material of low velocity fault zone to study its impact on the stress field.

In the following numerical experiments, we set the length of the low velocity fault zone to be the model length along X-axis, the depth and width of low velocity to be 3.6km and 2 km, respectively. We set the P-wave velocity to be $6000\ m/s$ and $3600\ m/s$ in the host rock and the low velocity fault zone, respectively. Similarly, we plot its velocity structure and the corresponding stress status for one finite element layer in the model from the Y-Z plane.

In the first velocity structure we tested as shown in Figure 2.16, we reduce the P-wave velocity one by one element from the host rock to low velocity fault zone from both Y and Z axis direction.

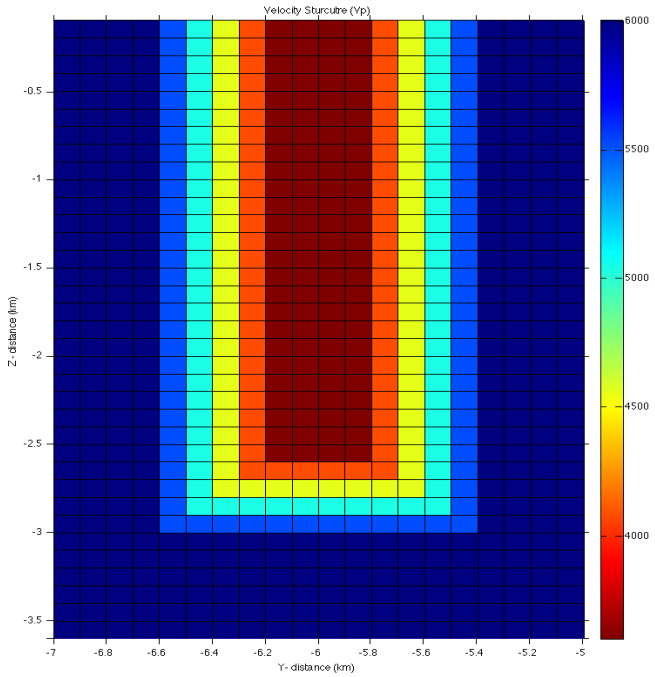

Figure 2.16: Velocity structure 1

When the system reaches static equilibrium, we plot one cross section layer of finite element in the model from Y-Z plane shown in Figure 2.17. One can observe that the range of stress ratio around the low velocity fault zone has reduced comparing to that in Figure 2.14. The ratio σ_{11}/σ_{33} has been reduced to $[0.9, 1.4]$ in Figure 2.17 (a) on the interface between the low velocity fault zone and its host rock compared to [0.6, 1.8] as shown in Figure 2.14 (a). The ratio σ_{12}/σ_{33} has been reduced to $[-0.3, -0.58]$ in Figure 2.17 (d) on the interface between the low velocity fault zone and its host rock compared to [-0.25, -0.65] as shown in Figure 2.14 (d).

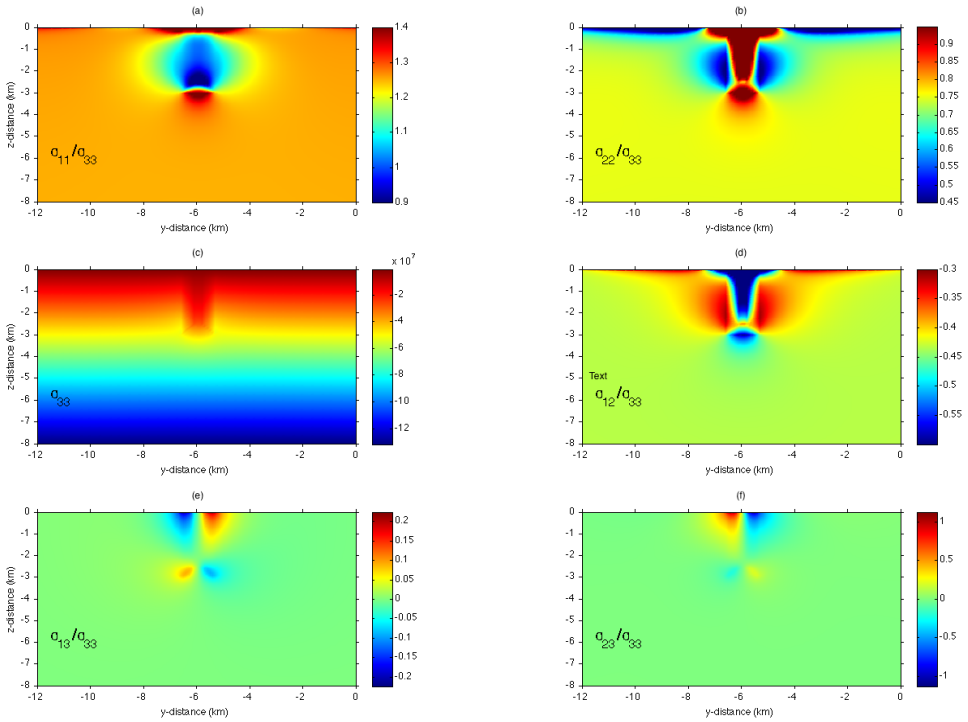

Figure 2.17: Stress status based on velocity structure 1. Cross section of stress status with free surface loading normalized by σ_{33}. σ_{11} corresponding to σ_{xx}, σ_{22} corresponding to σ_{yy} and σ_{33} corresponding to σ_{zz}, respectively.

Though the overall range of stress ratio has been largely reduced, one can still observe relative large stress ratio change along Z-axis. Hence, we further improve the velocity structure by add one more transitional layer along the Z-axis within the low velocity fault zone as shown in Figure 2.18.

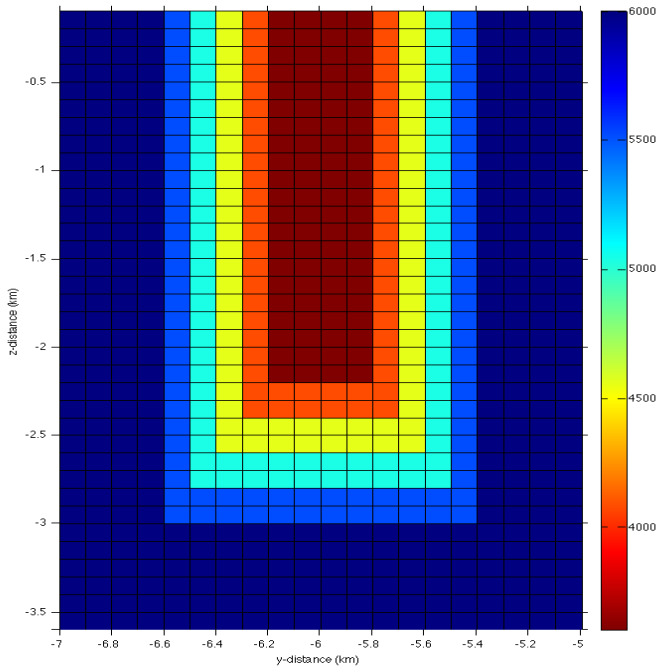

Figure 2.18: Velocity structure 2

Similarly, we plot one cross section layer of finite element in the model from Y-Z plane shown in Figure 2.19. It is quite clear that the velocity structure has been reflected by stress heterogeneity in Figure 2.19 as one can observe the boundaries between different layers as shown in Figure 2.19 (a), (b) and (d). The stress heterogeneity within the transitional layers along Z-axis has been improved compared to that in Figure 2.17.

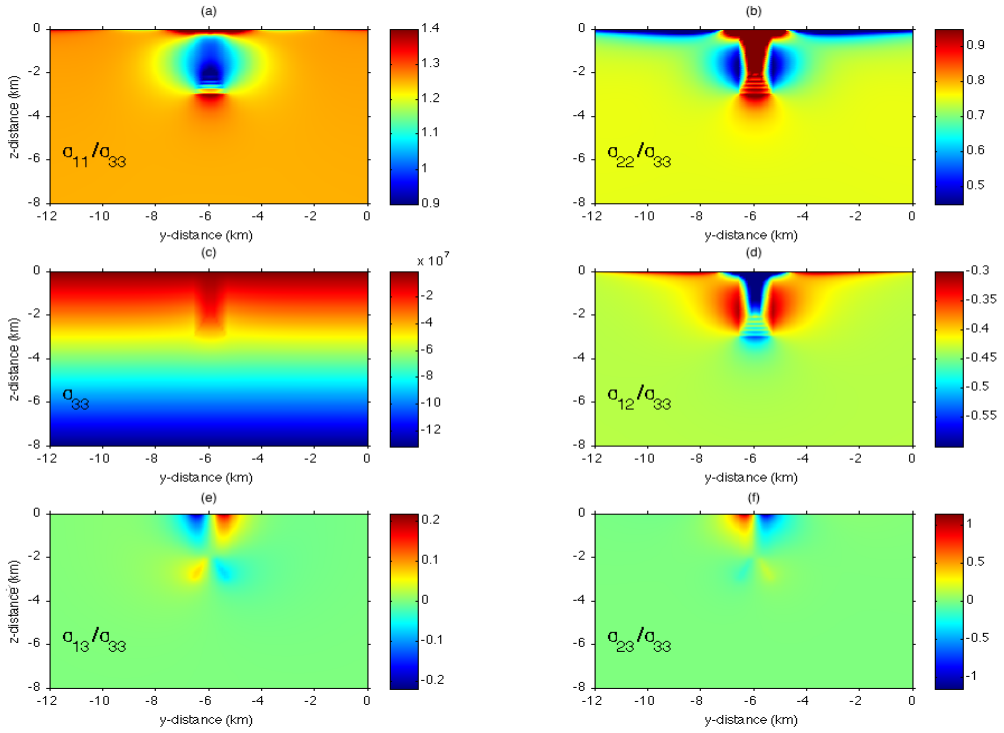

Figure 2.19: Stress status based on velocity structure 2. Cross section of stress status with free surface loading normalized by σ_{33}. σ_{11} corresponding to σ_{xx}, σ_{22} corresponding to σ_{yy} and σ_{33} corresponding to σ_{zz}, respectively.

In order to further improve the stress heterogeneity along Z-axis, we add two more transitional layers along the Z-axis within the low velocity fault zone as shown in Figure 2.20.

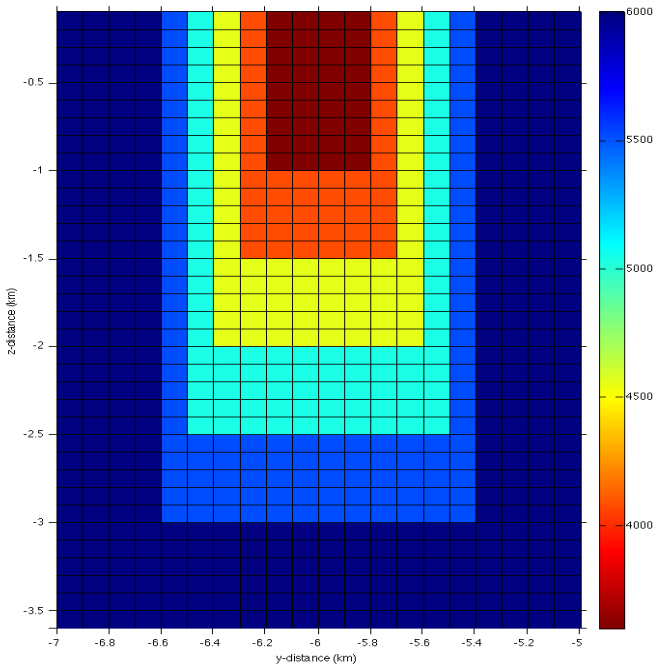

Figure 2.20: Velocity structure 3

The cross section layer of finite element in the model from Y-Z plane has been shown in Figure 2.21. One can observe relatively smooth change of stress ratio between the layers with different P-wave velocity within the low velocity fault zone along Z-axis.

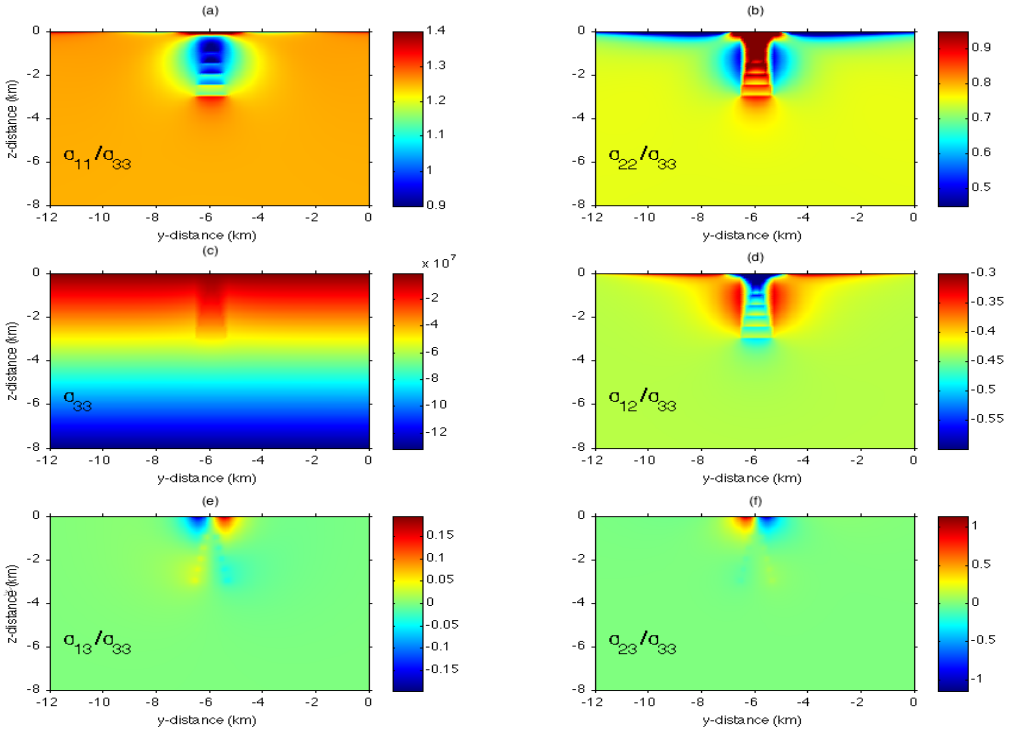

Figure 2.21: Stress status based on velocity structure 3. Cross section of stress status with free surface loading normalized by σ_{33}. σ_{11} corresponding to σ_{xx}, σ_{22} corresponding to σ_{yy} and σ_{33} corresponding to σ_{zz}, respectively.

In this section, we applied the boundary loading technique into the inhomogeneous model with low velocity fault zone. We presented substantial numerical experiments to study the effect of geometrical and physical quantities of low velocity fault zone on it surrounding stress field. We found that the stress heterogeneity around low velocity fault zone is very sensitive to its location, shape and velocity structure. Overall, we presented a viable way to calculate the stress field for inhomogeneous model through a dynamic solver.

We will then apply the dynamic relaxation technique in the next section for the elasto-

plastic dynamic rupture modeling to investigate the inelastic response of compliant fault zones to the nearby earthquake.

3. THE INELASTIC RESPONSE OF CALICO AND RODMAN FAULT ZONES TO THE 1992 LANDERS EARTHQUAKE

In the previous chapter, we have obtained the initial stress field for the compliant fault zones through the dynamic relaxation technique. In this chapter, we will study the inelastic responses of the compliant fault zones to the nearby earthquake through an elastoplastic and dynamic modeling. Specifically, we will investigate the inelastic response of the Calico and Rodman fault zones to the 1992 Landers Earthquake and compare the simulation results with the Interferometric synthetic aperture radar (InSAR) data.

The June 28 1992, Mw 7.3 Landers earthquake was the largest earthquake in southern California in several decades. It occurred in the Mojave Desert in southern California, which is dominated by a series of right lateral strike-slip faults with the Eastern California Shear Zone (ECSZ). The responses of compliant fault zones to the Landers rupture have attracted a great deal of attention during the past decades. Several studies indicate that some portion of the compliant fault zone exhibits inelastic response while the rest shows elastic response [e.g. Vidale and Li, 2003; Kang, 2014; Kang and Duan, 2015]. Hence, we choose the elastoplastic modeling over the elastic modeling in our numerical simulation.

For the elastoplastic modeling, one of the most important steps is to obtain the stress field over the whole model region, especially within the compliant fault zone. Our dynamic modeling is composed of two steps: dynamic relaxation and dynamic simulation. In the dynamic relaxation step, we apply the same boundary loading technique to obtain the desired stress field over the whole model region. The boundary condition in dynamic simulation will be the same as in the dynamic relaxation process. Additionally, we need to pass not only the stress field but also the displacement field from dynamic relaxation process to dynamic simulation process. In our spontaneous rupture modeling, boundary

loading might cause faults to slide during dynamic relaxation process. In order to avoid the movement of these sub-faults, we need to "lock" them during dynamic relaxation process and "unlock" them at the beginning of dynamic simulation. Here by "lock" we refer to assigning large enough static frictional coefficient on fault nodes. After the system reaches static equilibrium, we obtain the desired stress filed over the whole model region and start the dynamic simulation process.

3.1 Model setup

In our numerical model, we simplify the complicated Landers rupture fault system into three segments: Johnson Valley fault, Emerson fault and Camp Rock fault from southeast to northwest. In addition, we ignore the overlapping between sub-faults of the Landers fault system. The mapview of the three non-overlapping fault segments on the surface of 3D modeling are shown in Figure 3.1.The azimuth of the three segments are given as 350° for Johnson Valley fault, 332° for Emerson fault and 316° for Camp Rock fault, respectively.

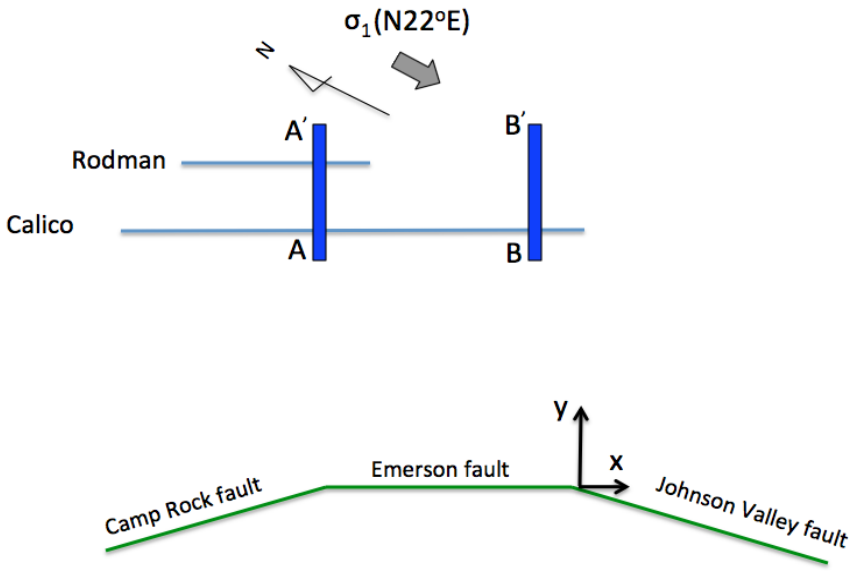

Figure 3.1: Numerical modeling of the Landers earthquake. The origin of coordinate system locates at the interception between Emerson fault and Johnson Valley fault. Three fault segments marked in green, two compliant fault zones marked in light blue which are parallel to the Emerson fault. Profiles AA' and BB' will be explored in details in Figure 3.7.

In the finite element modeling, we apply the mesh degeneration technique introduced in Hughes (2012) for the meshing of the three-segment branching fault. We set the azimuth of Camp Rock fault to 314° to keep the same branch angle ($\theta = 18^\circ$) for both Johnson Valley fault and Camp Rock fault for simplicity in mesh generation. In our finite element modeling, the mesh size along x and z direction is set to be 500 m, and 162.5 m along y direction which is calculated by $dx \times \tan(\theta)$. The size of the whole model is given by

$x \in [-80\ km, 80\ km], y \in [-40\ km, 40\ km], z \in [-30\ km, 0]$.

Two compliant fault zones Calico and Rodman are parallel with each other and are located northeast of the Emerson fault as shown in Figure 3.1, respectively. The Calico fault zone is about 2 km wide along y-axis, 4 km deep along z-axis and 20km long along x-axis starting from the middle of Camp Rock fault and ending in the middle of Emerson fault. The Rodman fault zone is about 2km wide along y-axis, 2 km deep along z-axis and 40km long along x-axis starting from the middle of Camp Rock and ending in the middle of Johnson Valley fault.

The material parameters of the compliant fault zones in this model are given as follows:

1. Density: ρ = 2.67$\times 10^3\ kg/m^3$
2. P-wave velocity: V_P = 2.4 $\times 10^3\ m/s$
3. S-wave velocity: V_S = 1.368 $\times 10^3\ m/s$
4. Internal frictional angle $\tan(\phi)$: 0.58
5. Cohesion: 0.1 MPa

The material parameters of the intact rocks in this model are given as follows:

1. Density: ρ = 2.67$\times 10^3\ kg/m^3$
2. P-wave velocity: V_P = 6.0 $\times 10^3\ m/s$
3. S-wave velocity: V_S = 3.464 $\times 10^3\ m/s$
4. Internal frictional angle $\tan(\phi)$: 0.85
5. Cohesion: 20 MPa

In this model, we add velocity structure for both compliant fault zones and the host rocks for better simulation results following Cochran et al. [2009]. We plot a cross section of the model to view the velocity structure implemented in our modeling as shown in Figure 3.2. Note that in the cross section view we only plot the velocity structure around the compliant fault zones instead of the whole model. Besides, the cross section plane is chosen for x within $[-50\ km, -30\ km]$ to cover both compliant fault zones since they have different length along x-axis.

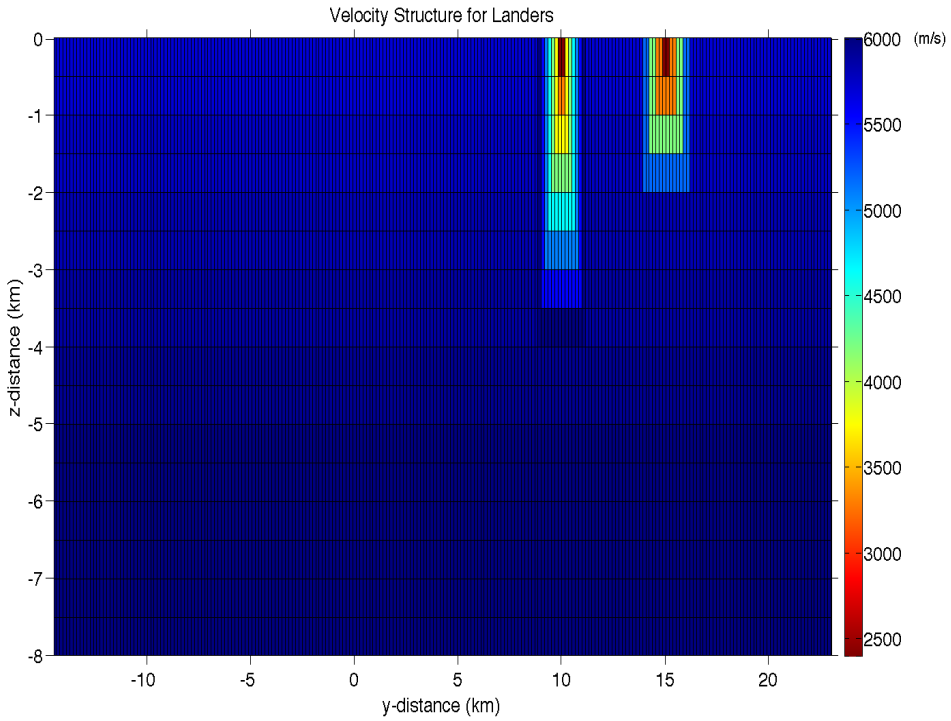

Figure 3.2: Velocity structure for the Landers model along profile AA'

In Figure 3.2, one can observe that the velocity structure is depth dependent for host rocks and gradually reduced for compliant fault zones similar to Figure 4 (A) in Cochran

et al. [2009].

The stress orientation we choose for the elastoplastic modeling is $N22^{\circ}E$, which is reported in Hauksson [1994] through seismicity analysis in this region from 1981 to 1991. The desired stress field for the dynamic modeling is given in the following:

$$\sigma_{11} = 0.913\sigma_{33} \tag{3.1}$$

$$\sigma_{22} = 1.086\sigma_{33} \tag{3.2}$$

$$\sigma_{12} = -0.492\sigma_{33} \tag{3.3}$$

$$\sigma_{13} = \sigma_{23} = 0 \tag{3.4}$$

We apply the similar boundary loading dynamic relaxation technique to generate the stress field for our dynamic modeling. After the dynamic relaxation step is finished, we obtain the stress field for the whole model region. In order to visualize the initial stress field for dynamic simulation, we plot the same cross section as in the velocity structure in Figure 3.3.

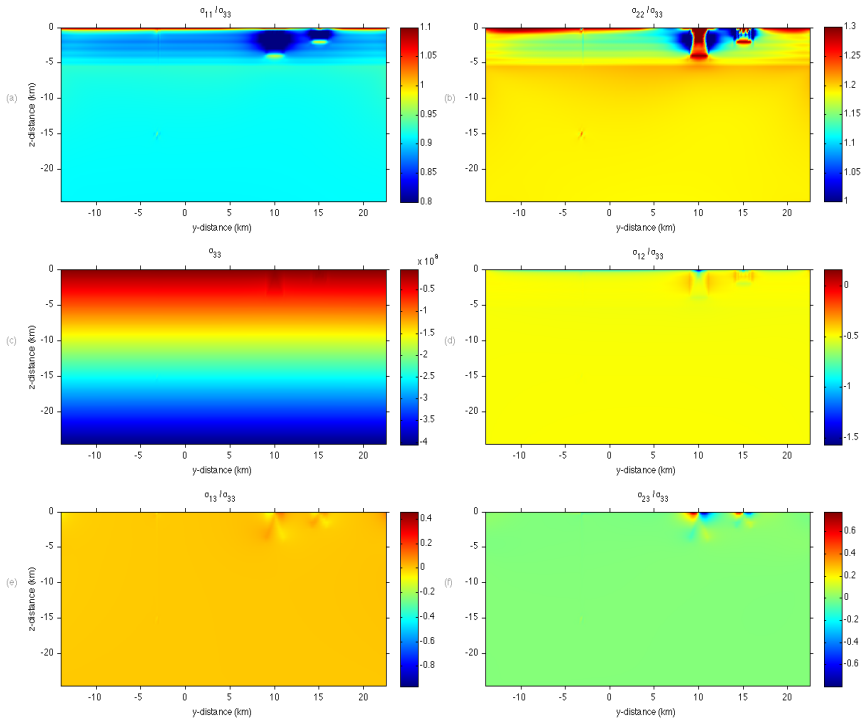

Figure 3.3: Cross section of stress field after dynamic relaxation along profile AA'

One can observe clear stress heterogeneity around compliant fault zones as well as the host rocks corresponding to their velocity structures as shown in Figure 3.3.

3.2 Rupture process and final slip distribution on faults

The response of compliant fault zones to nearby rupture normally refers to small scale displacement field, which is largely determined by the rupture propagation and slip distribution on fault. Specifically, the small scale displacement around the compliant fault zones is controlled by its dynamic stress perturbation during rupture process. In order to study the response of compliant fault zones to the nearby Landers rupture, we first need to verify that the rupture process and final slip distribution on the faults from our numerical results are consistent with the inversion results reported in Cohee and Beroza [1994] and

Wald and Heaton [1994].

In our numerical modeling, the location of the three subfaults are given in following (also shown in Figure 3.1):

Johnson Valley fault

$(x, y, z) \in [-50\ km, -20.5\ km] \times [-9747.6\ km, -162.5\ km] \times [-15\ km, 0\ km]$;

Emerson fault

$(x, y, z) \in [-20\ km, 0\ km] \times [0\ km, 0\ km] \times [-15\ km, 0\ km]$;

Camp Rock fault

$(x, y, z) \in [0.5\ km, 28\ km] \times [-9097.7\ km, -162.5\ km] \times [-15\ km, 0\ km]$.

After the system reaches static equilibrium, we obtain the stress field over the whole model region. Then we follow the idea introduced in Day et al. [2005] to calculate the stress on the three fault segments from the element stress in the elastoplastic modeling as it plays an important role in rupture propagation and on fault slip distribution on fault. The final slip distribution is determined by the shear stress drop on the faults. The rupture propagation is determined by the seismic S value defined in Day [1982]:

$$S = \frac{|\sigma_n|\mu_s - \tau_0}{\tau_0 - |\sigma_n|\mu_d} \tag{3.5}$$

where σ_n denotes the normal stress on fault, τ_0 denotes the initial equilibrium value of traction, μ_s denotes the static frictional coefficient, μ_d denotes the dynamic frictional coefficient. Note that the slip weakening frictional law is applied in our numerical simulation. According to Day [1982], the large S value will lead to slow dynamic rupture propagation speed.

The on fault stress calculated from element stress over the whole model region is not totally uniform mainly due to two facts: first, the stress heterogeneity in the shallow part

of the model as shown in Figure 3.3; second, the stress heterogeneity caused by the Calico and Rodman fault zones which was not to far away from the three fault segments as shown in Figure 3.3. Thus, we need to manually choose appropriate frictional coefficients on different parts of different fault segments according to the S value defined in Equation (3.5) in order to match the inversion results. In addition, we add certain amount of cohesion on the shallow part of the model to avoid abnormal behavior of rupture due to the stress heterogeneity on surface.

In the dynamic simulation process, we nucleate the Landers rupture at about 7.5 km deep along Johnson Valley fault and terminate it at 35 s when the slip on fault reaches the static value. The rupture propagates about 10 km in Southeast direction before it stops. Along Northwest direction, it propagates and jumps over to the Emerson fault. It accelerates along Emerson fault and finally jumps to Camp Rock fault before it arrests as shown in Figure 3.4. The magnitude of Landers earthquake in our simulation is 7.312 M_w. Note that the contour interval is 0.5 s in Figure 3.4. To sum up, the rupture travels around 78 km and 15 km along strike and dip direction, respectively.

As for the final slip distribution, the largest final slip is about 6 m in all three segments and occurs in the Emerson fault although the rupture is initiated at Johnson Valley fault. On Johnson Valley fault, the largest final slip occurs at the northeast part instead of its nucleation center; On Emerson fault, the largest slip occurs in the left center with the largest magnitude around 6 m. On Camp Rock fault, the largest slip occurs on the right center close to Emerson fault.

Compare to the inversion result in Figure 3.5 (reported in Cohee and Beroza [1994] and Wald and Heaton [1994]), the magnitude and main features of final slip distribution are preserved in our numerical results although there are some mismatch in the deep part of Johnson Valley and Camp Rock fault.

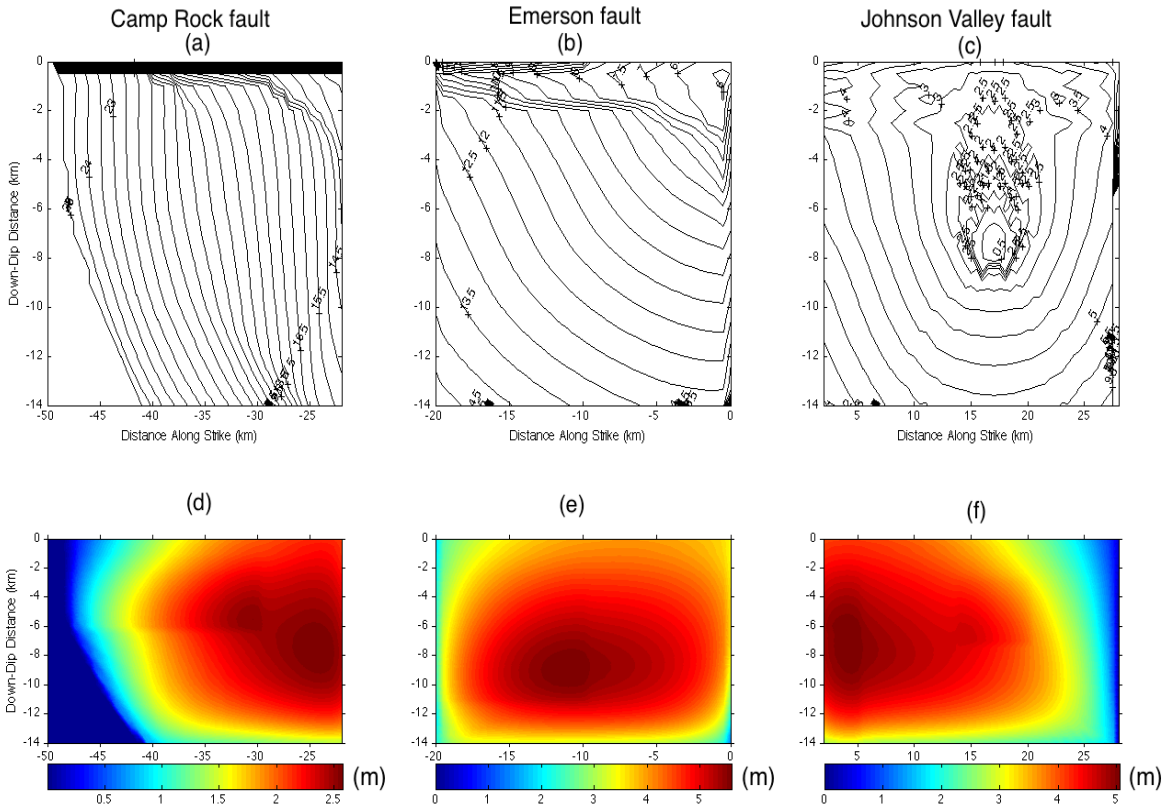

Figure 3.4: Rupture contour and final slip distribution in our numerical model. Rupture contours (a,b,c) and final strike-slip (d,e,f) on Camp Rock, Emerson and Johnson Valley fault are plotted on top and bottom, respectively. Contour interval is 0.5 s.

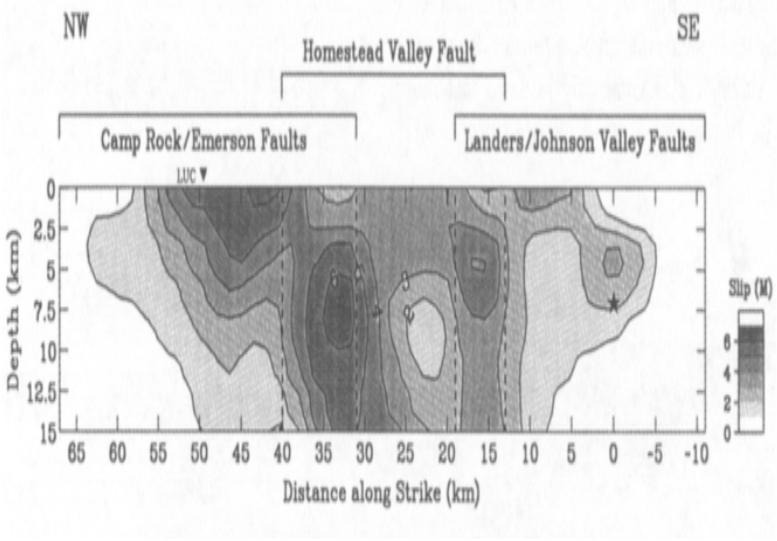

Figure 3.5: Inversion result of final slip distribution on the Landers faults reported in Wald and Heaton [1994]

3.3 Numerical results of surface displacement around compliant fault zones and comparison with InSAR data in the ECSZ

After dynamic simulation process is finished, the next step is to study the inelastic response of Calico and Rodman fault zones to the Landers rupture. In order to investigate the surface displacement caused by the compliant fault zones, we need to perform two numerical models, one with compliant fault zones and the other not. Then we subtract the displacement field between the two numerical models to generate the residual displacement field. The residual displacement field will show the impact of the compliant fault zones to the nearby earthquake.

We name the modeling with compliant fault zone target model and the other one reference model. The only difference between the two models is that the reference model is

composed of homogeneous material.

The inelastic response in the numerical modeling is determined by Drucker-Prager criterion when calculate the plastic strain accumulate over time steps. The parameter for plastic yielding is given in the following:

1. Internal frictional angle $\tan(\phi)$: 0.85 (intact rocks) V.S. 0.58 (compliant fault zones)

2. Cohesion: 20 MPa (intact rocks) V.S. 0.1 MPa (compliant fault zones)

After we finish the numerical simulation for the two models and subtract them to obtain the residual displacement on model surface. Note that the residual displacement is a three dimensional vector field.

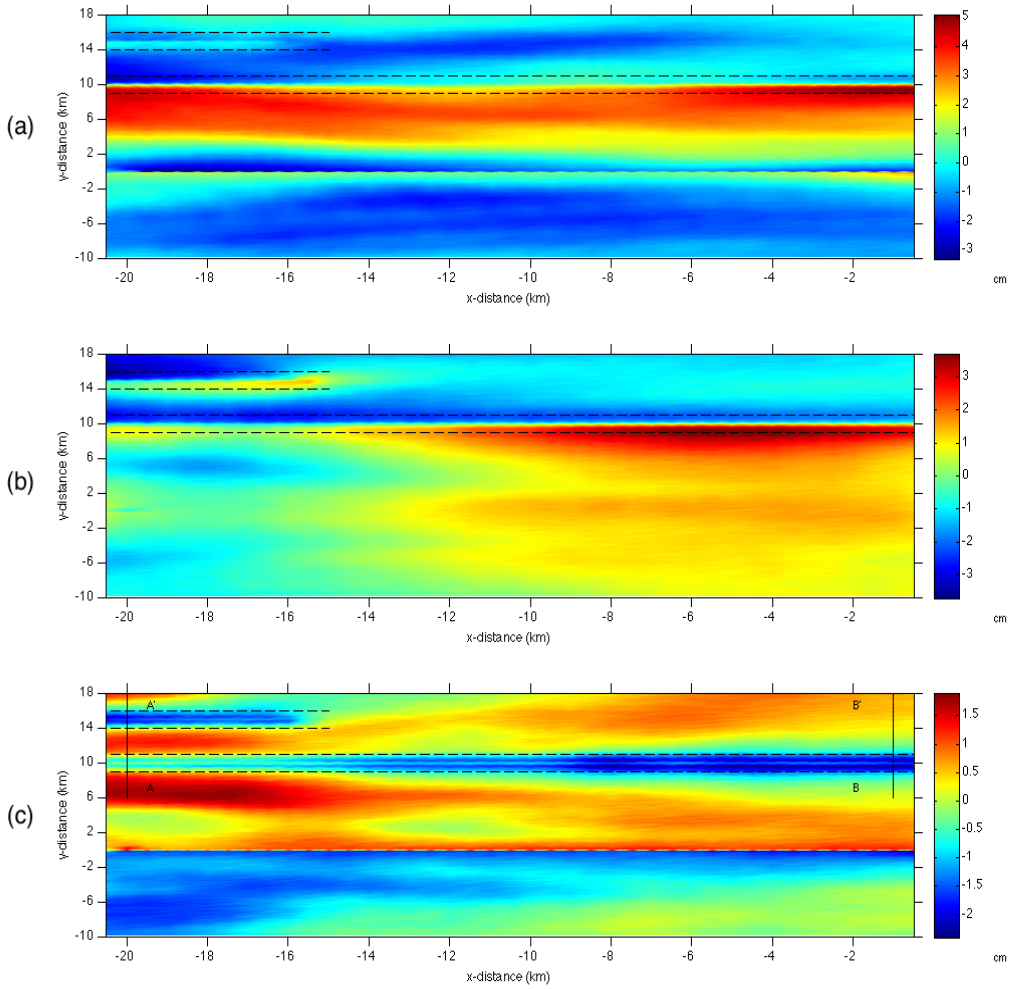

Figure 3.6: Residual displacement along X, Y and Z directions on the Earth's surface induced by the Landers earthquake

In Figure 3.6, we plot the residual displacement induced by Landers earthquake on the model surface around Emerson fault, Calico and Rodman fault zones. In Figure 3.6 (a) - (c), we show the x component, y component and z component of the residual displacement, respectively. Note that the black dash line denotes the fault zones in Figure 3.6. One can

observe clear difference in different residual displacement components from the magnitude shown in the color bar in Figure 3.6. In the residual displacement along z direction as shown in Figure 3.6 (c), one can observe clear subsidence within Calico and Rodman fault zones. In addition, the subsidence in compressional quadrant around BB' profile is enhanced compared to that in the extensional quadrant.

In order to compare the residual displacement with the Interferometric Synthetic Aperture Radar (InSAR) data, we need to convert it into the same dimension first. InSAR data is recorded by satellites which continuously measure the small scale deformation changes. Specifically, we will choose the satellite's Line of Sight (LOS) displacement in the comparison. The formula to calculate LOS displacement reported in Fialko et al. [2001] is given as the following:

$$d_{los} = [U_n \sin(\varphi) - U_e \cos(\varphi)] \sin(\lambda) + U_u \cos(\lambda) + \delta_{los} \tag{3.6}$$

where d_{los} denotes the LOS displacement, λ denotes the satellite radar incidence angle, φ denotes the azimuth of the satellite heading vector, δ_{los} denotes the measurement error, U_n, U_e, U_u represent the residual displacement along north, east and vertical up direction, respectively.

For the satellite radar incidence angle λ and the azimuth of the satellite heading vector φ, we refer to the previous studies about the 1992 Landers earthquake [e.g. Fialko, 2004; Cochran et al., 2009; Barbot et al., 2009] where $\lambda = 23^\circ$ and $\varphi = 188.55^\circ$.

After all the variables needed in the formula (3.6) are collected, we plot the LOS displacement from our numerical modeling as shown in Figure 3.7.

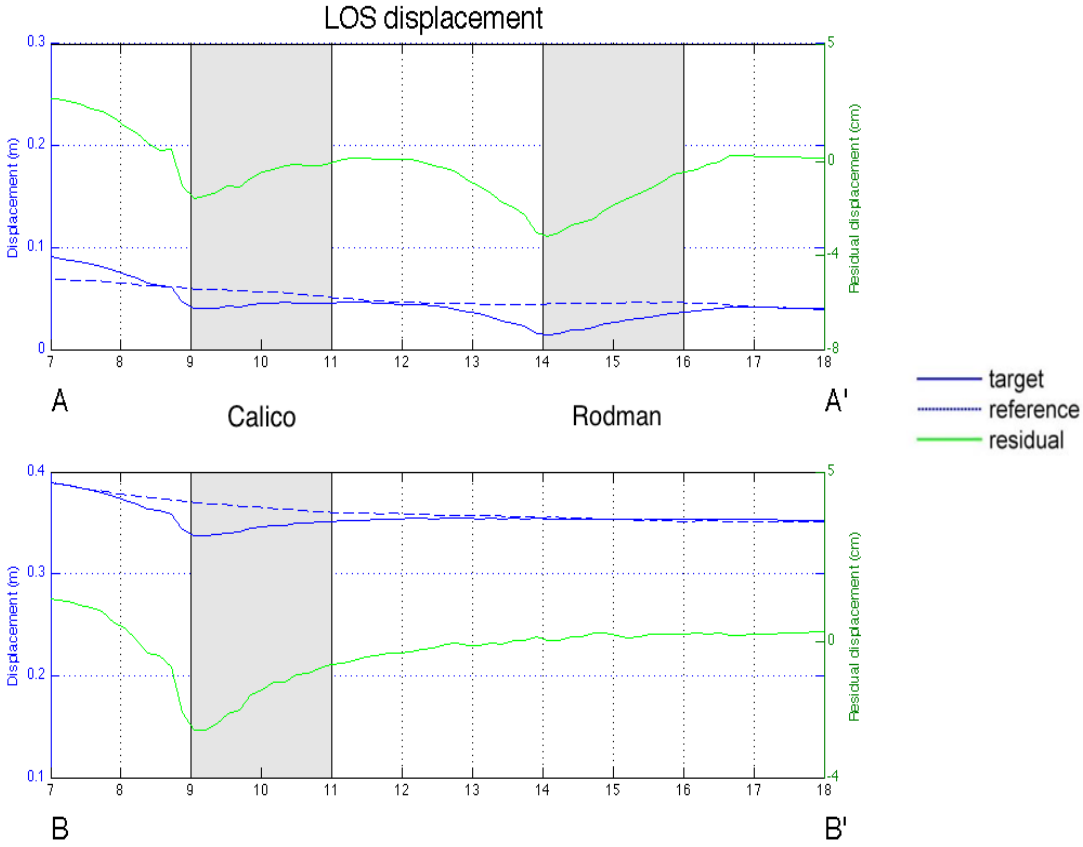

Figure 3.7: Residual displacement along profile AA' and BB', synthetic to InSAR LOS direction. Residual displacement marked in green curve with unit centimeter on right axis, target and reference models are marked in solid and dash blue with unit meter on the left axis. The shaded bands represent the compliant fault zones.

In Figure 3.7, we plot the residual displacement along profile AA' and BB' in green curve with centimeter unit on the right axis and the displacement from target and reference model in solid and dash blue on the left axis with meter unit.

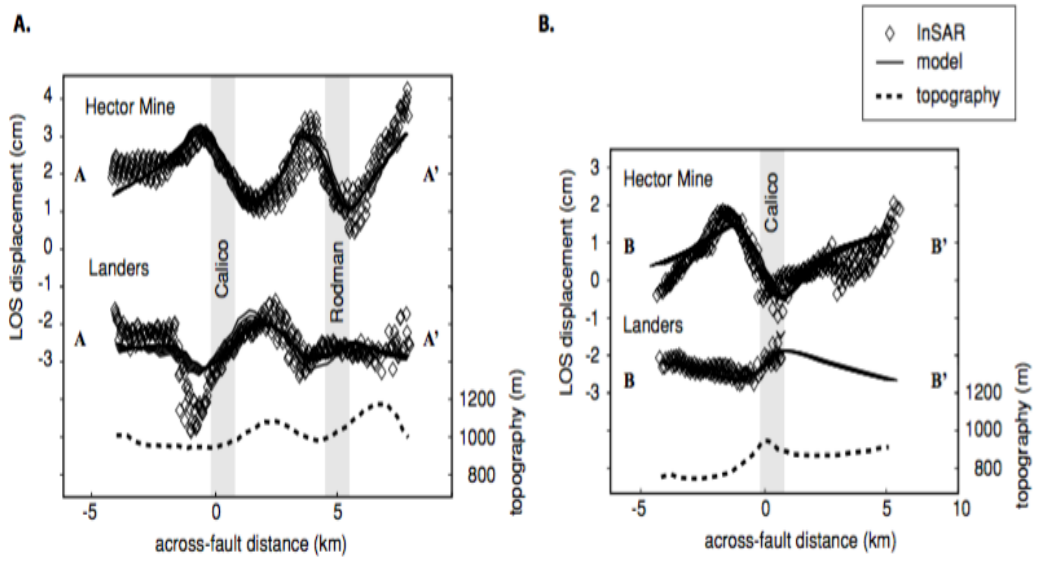

Figure 3.8: InSAR LOS displacement along profile AA' and BB' reported in Barbot et al. [2009]

Compare to the InSAR observation data shown in Figure 6(a) of Barbot et al. [2009], our synthesized LOS displacement preserve the same magnitude and same trend in general. Compare to the results from elastic modeling in Figure 6(a) of Barbot et al. [2009] , our synthesized LOS displacement fit the InSAR data better especially around the compliant fault zones. Specifically, our synthesized LOS displacement around AA' profile on the left side of Calico fault zone matches the InSAR observation data better in term of magnitude as shown in Figure 3.7.

However, our synthesized LOS displacement along AA' profile near Rodman fault zone is larger than that in the InSAR observation. The possible reason is that the velocity reduction in Rodman is to high. The same issue also exists around the Calico fault zone along BB' profile. Hence, in order to better fit the InSAR observation data, we modify the velocity structure in the Calico and Rodman fault zones. We reduce only 30% of body

wave velocity in Rodman fault zone and right half of Calico fault zone close to BB' profile as shown in Figure 3.9 and 3.10.

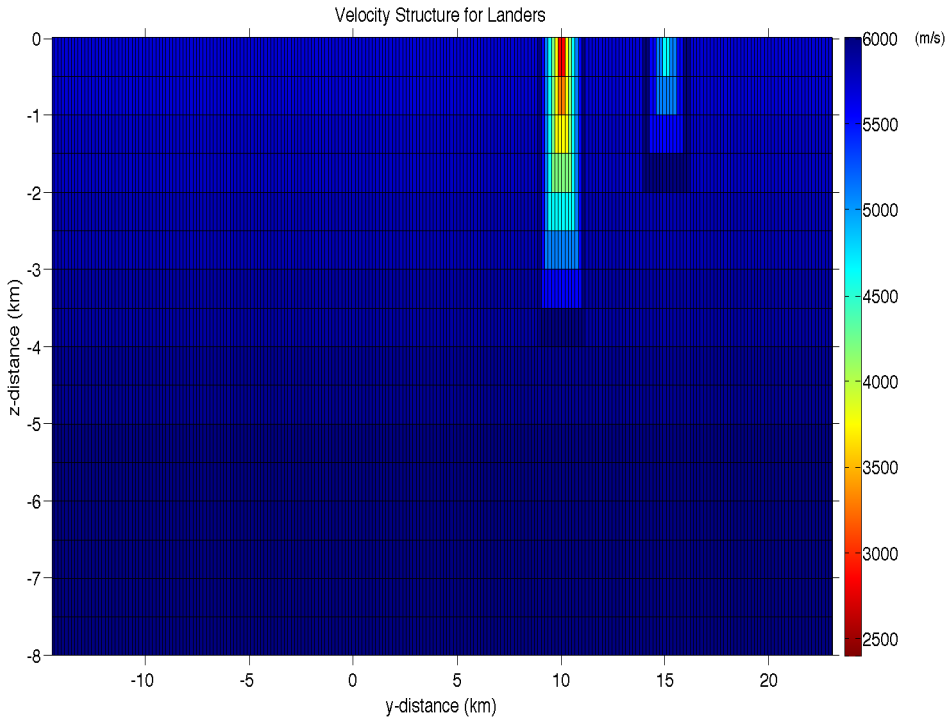

Figure 3.9: Velocity structure for the Landers model along AA' profile

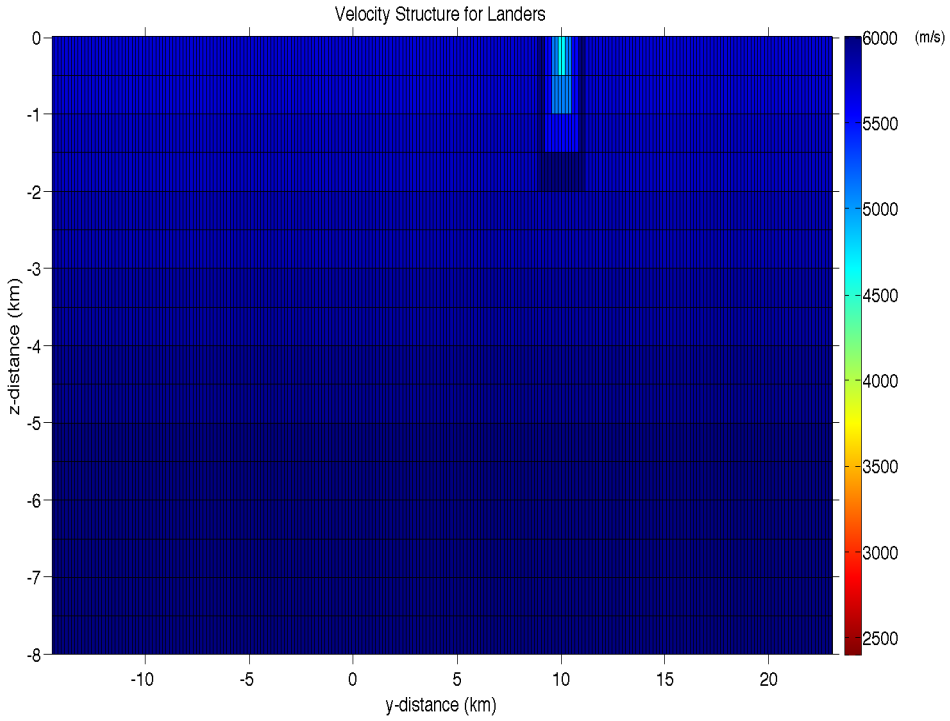

Figure 3.10: Velocity structure for the Landers model along BB' profile

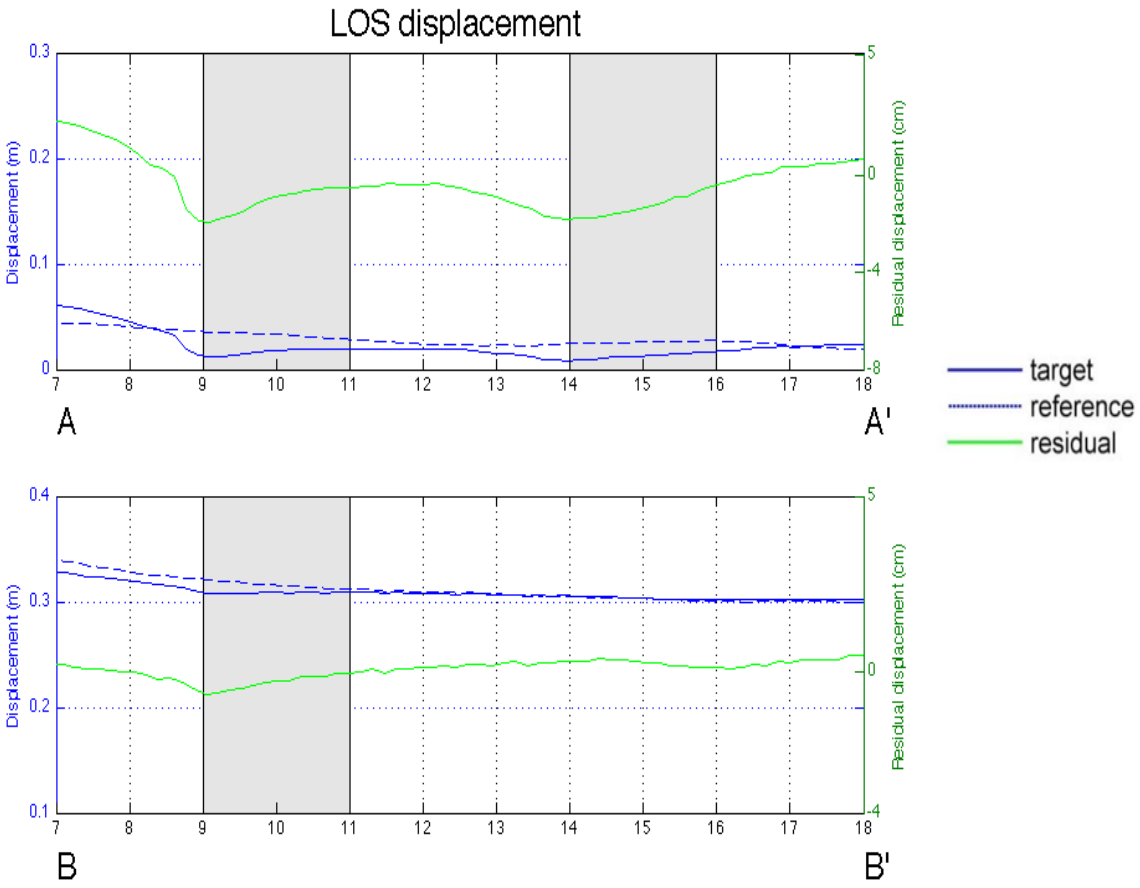

Figure 3.11: Residual displacement along profile AA' and BB' with velocity structure in Figure 3.9 and 3.10, synthetic to InSAR LOS direction. Residual displacement marked in green curve with unit centimeter on right axis, target and reference models are marked in solid and dash blue with unit meter on the left axis. The shaded bands represent the compliant fault zones.

In Figure 3.11, our synthesized LOS displacement along AA' near Rodman fault zone and along BB' profile near Calico fault zone got improved compared to the InSAR observation data. In order to further compare our synthesized LOS displacement and InSAR observation data, we plot them into the same figure as shown in Figure 3.12. Since we do

not have the InSAR observation data, we use a software to extract the data points reported in Barbot et al. [2009]. From Figure 3.12, one can observe that our synthetic results have a very good match with the InSAR observation data on the left side of Calico fault zone. In addition, our synthetic results also preserve the same trend on the right side of Calico fault zone and on both sides of Rodman fault zone.

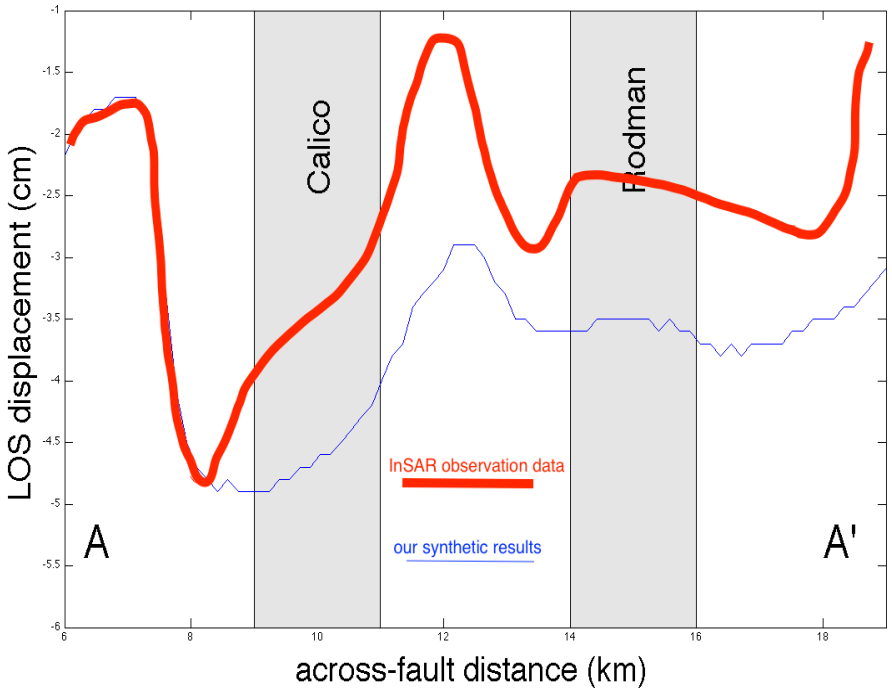

Figure 3.12: Comparison between InSAR observation data and our synthetic residual displacement along profile AA' and BB' with velocity structure in Figure 3.9 and 3.10

In order to the show the effect of inelastic modeling, we compare the results between our elastoplastic modeling and elastic modeling with homogeneous initial stress field. In the elastic modeling, homogeneous stress on fault segments is assigned and no element

stress stress is assigned within the model.

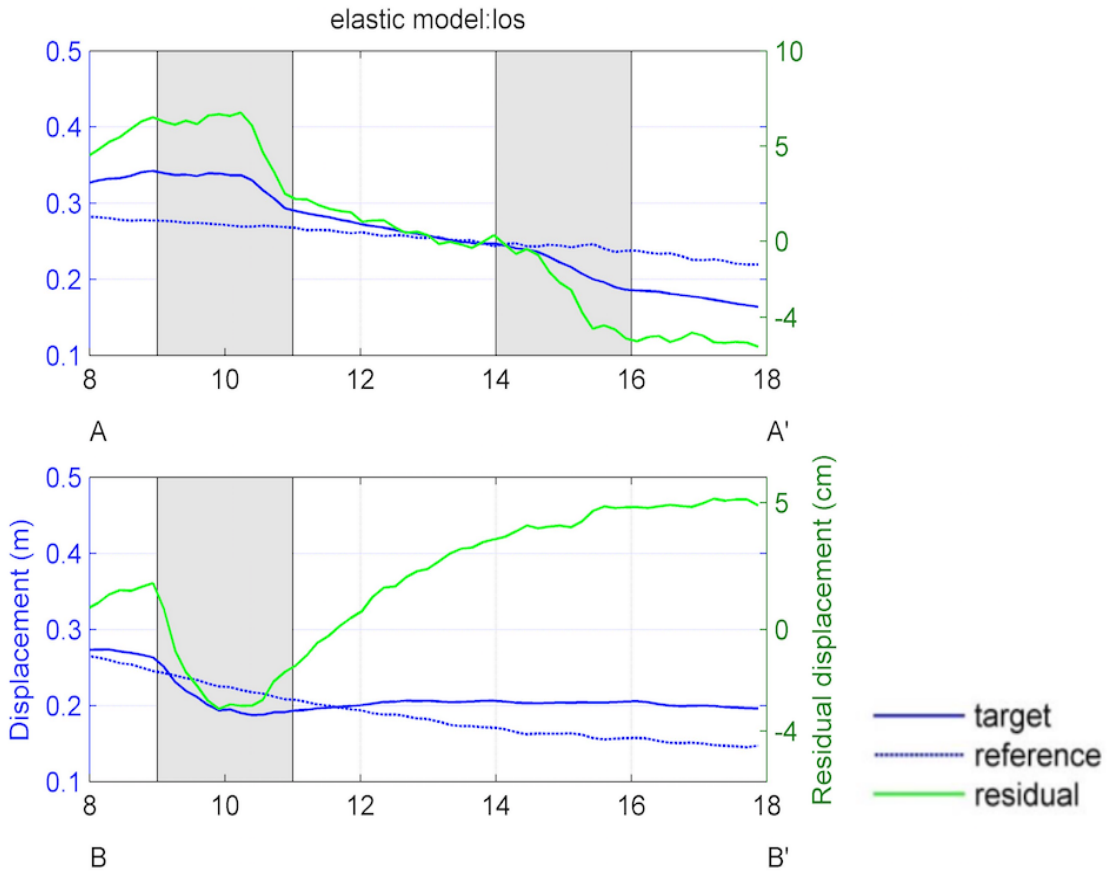

Figure 3.13: Residual displacement along profile AA' and BB' with elastic modeling with homogeneous initial stress on fault segments

Compare to the InSAR observation data, the synthetic LOS displacement from our elastoplastic model fits much better than that of the elastic model with homogeneous initial stress on fault segments, especially around the compliant fault zones. Around 1km left of Calico fault zone, the LOS displacement of InSAR observation data has a "V" shape change while the results from elastic model show different patterns. In addition, the LOS

displacement of InSAR observation data increases within the Calico and Rodman fault zones while the synthetic LOS displacement from the elastic model decreases within the two compliant fault zones.

Furthermore, we will compare our results with that of the similar elastoplastic modeling reported in Kang [2014] as shown in Figure 3.14. In that model, the homogeneous initial stress field within the model is assigned based the stress orientation over the whole model, including the compliant fault zones. Our synthesized LOS displacement fit the InSAR observation data better, especially around the compliant fault zones. This indicates that the initial stress field around the compliant fault zones plays a very important role in the response of compliant fault zones to the nearby earthquakes.

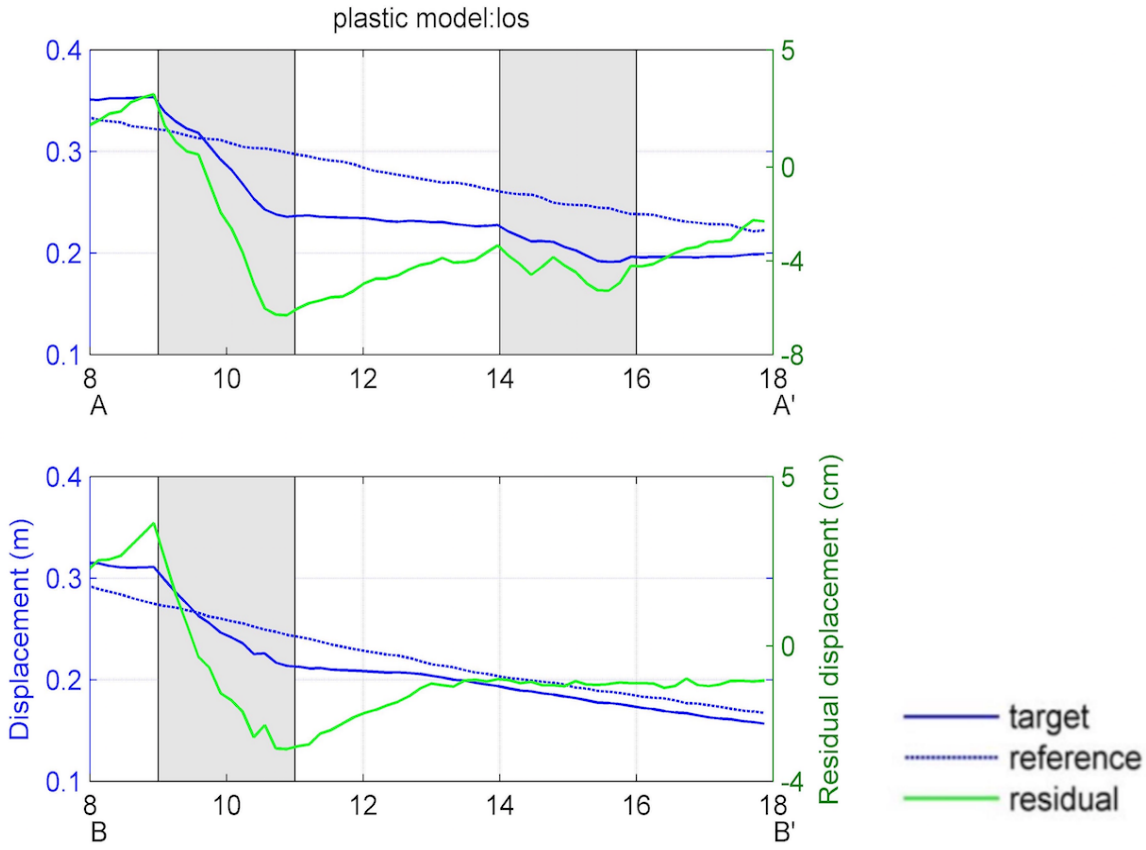

Figure 3.14: Residual displacement along profile AA' and BB' with elastoplastic models with homogeneous initial stress field reported in Kang [2014]

In this chapter, we apply the dynamic relaxation technique to obtain the stress field for Landers earthquake modeling. We study the inelastic response of Calico and Rodman fault zones to the Landers earthquake through an elastoplastic dynamic rupture model. The rupture propagation and final slip distribution on three fault segments are consistent with inversion results of Landers earthquake from previous studies. Our synthesized LOS displacement shows a good match with the InSAR data, suggesting the importance of incorporating the heterogeneous initial stress field obtained from dynamic relaxation

method.

4. SUMMARY AND CONCLUSIONS

In this thesis, we have studied and implemented a dynamic relaxation method to obtaining the stress field over the whole model region, especially for the inhomogeneous model. This dynamic relaxation method is mainly based on the continuous nodal force loading that is applied on the model boundary. The proposed method comes with two steps: first, apply appropriate boundary nodal force loading on the homogeneous model to obtain the desired stress field; additionally, apply the same boundary nodal force loading on the inhomogeneous model to get the stress field. We then develop an elastoplastic dynamic rupture model to investigate the inelastic response of the compliant fault zones to the nearby earthquake. The initial stress field for the elastoplastic modeling is generated through applying the dynamic relaxation technique on the same model till it reaches static equilibrium.

In Section 2, we first introduce the fixed end beam model with analytical solution to verify our dynamic relaxation method. We experimentally exhibit the accuracy of our numerical modeling through the error analysis between simulation results and analytical solution. After that, we apply the same boundary nodal force loading technique into the homogeneous model. By comparing with the desired stress field, the numerical results from the proposed method show high accuracy and efficiency. Then, we apply the same boundary nodal loading force to the same size inhomogeneous model to obtain the stress field over the whole model region. Despite the fact that we do not have the analytical solution for the inhomogeneous modeling, we present a viable approach to calculate the stress field for the inhomogeneous model.

In Section 3, we investigate the inelastic response of the Calico and Rodman fault

zones to the 1992 Landers earthquake through an elastoplastic dynamic rupture modeling. The initial stress field for dynamic simulation is obtained through the dynamic relaxation technique. The rupture propagation and final slip distribution on the Landers fault segments from the numerical modeling show a good match with inversion results from previous works in literature. Finally, our simulation results match the InSAR data well which indicates the heterogeneous initial stress field plays an important role in determining the response of Calico and Rodman fault zones to the Landers rupture.

REFERENCES

Andrews, D.J. (1976). Rupture velocity of plane strain shear cracks. *Journal of Geophysical Research*, 81(32):5679–5687.

Barbot, S., Y. Fialko, and D. Sandwell (2009). Three-dimensional models of elastostatic deformation in heterogeneous media, with applications to the eastern California shear zone. *Geophysical Journal International*, 179(1):500–520.

Belytschko, T., D. Organ, and Y. Krongauz (1995). A coupled finite element-element-free galerkin method. *Computational Mechanics*, 17(3):186–195.

Ben-Zion, Y. (1998). Properties of seismic fault zone waves and their utility for imaging low-velocity structures. *Journal of Geophysical Research: Solid Earth*, 103(B6): 12567–12585.

Ben-Zion, Y., and C.G. Sammis (2003). Characterization of fault zones. *Pure and Applied Geophysics*, 160(3-4):677–715.

Chester, F.M., and J.S. Chester (1998). Ultracataclasite structure and friction processes of the punchbowl fault, San Andreas system, California. *Tectonophysics*, 295(1):199–221.

Chester, F.M., J.P. Evans, and R.L. Biegel (1993). Internal structure and weakening mechanisms of the San Andreas fault. *Journal of Geophysical Research: Solid Earth*, 98 (B1):771–786.

Cochran, E.S., Y.G. Li, P.M. Shearer, S. Barbot, Y. Fialko, and J.E. Vidale (2009). Seismic and geodetic evidence for extensive, long-lived fault damage zones. *Geology*, 37(4): 315–318.

Cohee, B.P., and G.C. Beroza (1994). Slip distribution of the 1992 Landers earthquake and its implications for earthquake source mechanics. *Bulletin of the Seismological Society of America*, 84(3):692–712.

Day, S.A. (1965). An introduction to dynamic relaxation(dynamic relaxation method for structural analysis, using computer to calculate internal forces following development from initially unloaded state). *The Engineer*, 219:218–221.

Day, S.M (1982). Three-dimensional simulation of spontaneous rupture: the effect of nonuniform prestress. *Bulletin of the Seismological Society of America*, 72(6A):1881–1902.

Day, S.M., L.A. Dalguer, N. Lapusta, and Y. Liu (2005). Comparison of finite difference and boundary integral solutions to three-dimensional spontaneous rupture. *Journal of Geophysical Research: Solid Earth*, 110(B12).

Drucker, D.C., and W. Prager (1952). Soil mechanics and plastic analysis or limit design. *Quarterly of Applied Mathematics*, 10(2):157–165.

Duan, B. (2010a). Inelastic response of compliant fault zones to nearby earthquakes. *Geophysical Research Letters*, 37(16).

Duan, B. (2010b). Role of initial stress rotations in rupture dynamics and ground motion: a case study with implications for the Wenchuan earthquake. *Journal of Geophysical Research: Solid Earth*, 115(B5).

Duan, B. (2011). Reply to comment by Y. Fialko on deformation of compliant fault zones induced by nearby earthquakes: theoretical investigations in two dimensions. *Journal of Geophysical Research: Solid Earth*, 116(B12).

Duan, B., and S.M. Day (2008). Inelastic strain distribution and seismic radiation from rupture of a fault kink. *Journal of Geophysical Research: Solid Earth*, 113(B12).

Duan, B., and D.D. Oglesby (2006). Heterogeneous fault stresses from previous earthquakes and the effect on dynamics of parallel strike-slip faults. *Journal of Geophysical Research: Solid Earth*, 111(B5).

Duan, B., J. Kang, and Y.G. Li (2011). Deformation of compliant fault zones induced by nearby earthquakes: theoretical investigations in two dimensions. *Journal of Geophysi-*

cal Research: Solid Earth, 116(B3).

Fialko, Y. (2004). Evidence of fluid-filled upper crust from observations of postseismic deformation due to the 1992 MW7. 3 Landers earthquake. *Journal of Geophysical Research: Solid Earth*, 109(B8).

Fialko, Y., M. Simons, and D. Agnew (2001). The complete (3-d) surface displacement field in the epicentral area of the 1999 MW7. 1 Hector Mine earthquake, California, from space geodetic observations. *Geophysical Research Letters*, 28(16):3063–3066.

Fialko, Y., D. Sandwell, D. Agnew, M. Simons, P. Shearer, and B. Minster (2002). Deformation on nearby faults induced by the 1999 Hector Mine earthquake. *Science*, 297 (5588):1858–1862.

Hauksson, E. (1994). State of stress from focal mechanisms before and after the 1992 Landers earthquake sequence. *Bulletin of the Seismological Society of America*, 84(3): 917–934.

Hughes, T.JR. (2012). The finite element method: linear static and dynamic finite element analysis. *Courier Corporation*.

Hughes, T.JR., and G.M. Hulbert (1988). Space-time finite element methods for elastodynamics: formulations and error estimates. *Computer Methods in Applied Mechanics and Engineering*, 66(3):339–363.

Hulbert, G.M., and T.JR. Hughes (1990). Space-time finite element methods for second-order hyperbolic equations. *Computer Methods in Applied Mechanics and Engineering*, 84(3):327–348.

Ida, Y. (1972). Cohesive force across the tip of a longitudinal-shear crack and Griffith's specific surface energy. *Journal of Geophysical Research*, 77(20):3796–3805.

Kang, J. (2014). Deformation of compliant fault zones induced by nearby earthquakes: theoretical investigations in three dimensions and applications to the east California shear zone. *PhD dissertation*, Texas A&M University.

Kang, J. and B. Duan (2015). Elastic and inelastic responses of compliant fault zones to nearby earthquakes in three dimensions: a parameter-space study. *Geophysical Journal International*, 201(2):1195–1214.

Li, Y.G., J.E. Vidale, K. Aki, F. Xu, and T. Burdette (1998). Evidence of shallow fault zone strengthening after the 1992 M7. 5 Landers, California, earthquake. *Science*, 279 (5348):217–219.

Savage, H.M., and E.E. Brodsky (2011). Collateral damage: evolution with displacement of fracture distribution and secondary fault strands in fault damage zones. *Journal of Geophysical Research: Solid Earth*, 116(B3).

Scholz,C.H., N.H. Dawers, J.Z. Yu, M.H. Anders, and P.A. Cowie (1993). Fault growth and fault scaling laws: preliminary results. *Journal of Geophysical Research: Solid Earth*, 98(B12):21951–21961.

Sleep, N.H. (1995). Ductile creep, compaction, and rate and state dependent friction within major fault zones. *Journal of Geophysical Research: Solid Earth*, 100(B7): 13065–13080.

Timoshenko, S.P., and J.M. Gere (1972). Mechanics of Materials. *Van Nordstrand Reinhold company, New York*.

Vidale, J.E., and Y.G. Li (2003). Damage to the shallow landers fault from the nearby Hector Mine earthquake. *Nature*, 421(6922):524–526.

Wald, D.J., and T.H. Heaton (1994). Spatial and temporal distribution of slip for the 1992 Landers, California, earthquake. *Bulletin of the Seismological Society of America*, 84 (3):668–691.